

Great Balls of FIRE II: The evolution and destruction of star clusters across cosmic time in a Milky Way-mass galaxy

Carl L. Rodriguez^{1,2*}, Zachary Hafen³, Michael Y. Grudić^{4†}, Astrid Lamberts^{5,6},
Kuldeep Sharma¹, Claude-André Faucher-Giguère^{7,8}, Andrew Wetzel⁹

¹McWilliams Center for Cosmology and Department of Physics, Carnegie Mellon University, Pittsburgh, PA, 15213

²Department of Physics and Astronomy, University of North Carolina at Chapel Hill, 120 E. Cameron Ave, Chapel Hill, NC, 27599, USA

³Department of Physics and Astronomy, University of California Irvine, CA 92697, USA

⁴Carnegie Observatories, 813 Santa Barbara St, Pasadena, CA 91101, USA

⁵Laboratoire Lagrange, Université Côte d'Azur, Observatoire de la Côte d'Azur, CNRS, France

⁶Laboratoire Artemis, Université Côte d'Azur, Observatoire de la Côte d'Azur, CNRS, France

⁷Department of Physics & Astronomy, Northwestern University, Evanston, IL 60208, USA

⁸Center for Interdisciplinary Exploration & Research in Astrophysics (CIERA), Northwestern University, Evanston, IL 60208, USA

⁹Department of Physics & Astronomy, University of California, Davis, CA 95616

Accepted XXX. Received YYY; in original form ZZZ

ABSTRACT

The current generation of galaxy simulations can resolve individual giant molecular clouds, the progenitors of dense star clusters. But the evolutionary fate of these young massive clusters, and whether they can become the old globular clusters (GCs) observed in many galaxies, is determined by a complex interplay of internal dynamical processes and external galactic effects. We present the first star-by-star N -body models of massive ($N \sim 10^5 - 10^7$) star clusters formed in a FIRE-2 MHD simulation of a Milky Way-mass galaxy, with the relevant initial conditions and tidal forces extracted from the cosmological simulation. We select 895 ($\sim 30\%$) of the YMCs with $> 6 \times 10^4 M_\odot$ from Grudić et al. 2022 and integrate them to $z = 0$ using the Cluster Monte Carlo Code, CMC. This procedure predicts a MW-like system with 148 GCs, predominantly formed during the early, bursty mode of star formation. Our GCs are younger, less massive, and more core-collapsed than clusters in the Milky Way or M31. This results from the assembly history and age-metallicity relationship of the host galaxy: younger clusters are preferentially born in stronger tidal fields and initially retain fewer stellar-mass black holes, causing them to lose mass faster and reach core collapse sooner than older GCs. Our results suggest that the masses and core/half-light radii of GCs are shaped not only by internal dynamical processes, but also by the specific evolutionary history of their host galaxies. These results emphasize that N -body studies with realistic stellar physics are crucial to understanding the evolution and present-day properties of GC systems.

Key words: globular clusters: general – galaxies: star clusters: general – stars: black holes – galaxies: star formation – Galaxy: evolution

1 INTRODUCTION

The formation, evolution, and destruction of globular clusters (GCs) has been a subject of intense study for nearly a century. While the first GCs were observed well before the first galaxies beyond the Milky Way (MW), we now know that most galaxies with luminosities $\geq 3 \times 10^6 L_\odot$ or halo masses $\geq 10^9 M_\odot$ contain GCs (e.g., Harris et al. 2013, 2017). And although the exact formation scenarios for GCs are still a topic of debate, it is now thought that a significant

number of GCs are simply the byproduct of normal star formation in the early Universe, where the high gas pressures in young, spheroidal, and merging galaxies allows for the efficient conversion of stars into bound clusters (e.g., Kruijssen 2015). This suggests that the formation of GCs and other old star clusters at high z and the formation of young massive clusters (YMCs) in the local universe are driven by the same physical processes occurring in different galactic environments. Furthermore, the typical masses ($\sim 10^4 M_\odot - 10^6 M_\odot$), luminosities, and compact radii of GCs allow them to be resolved in both local and distant galaxies, providing a wealth of observational information about clusters across different galaxy types and morphologies (Brodie & Strader 2006). Because of this,

* carl.rodriguez@unc.edu

† NASA Hubble Fellow

GCs and other star clusters are an ideal probe of galaxy formation and assembly. And while still strongly dependent on the model for cluster formation and (in many cases) the specific implementation of subgrid physics, it is now possible to model the initial conditions of star clusters in both realistic galaxies and cosmological simulations as a function of their formation environments (e.g., Li et al. 2017; Pfeffer et al. 2018).

In concert with these advancements in our understanding of cluster formation, our ability to create realistic, fully collisional N -body models of clusters has also improved by leaps and bounds. The last decade has seen the first direct summation N -body simulation of old GCs with 10^6 stars (Wang et al. 2016b), while the latest generation of Monte Carlo N -body codes (e.g., Giersz et al. 2013; Pattabiraman et al. 2013; Rodríguez et al. 2022) have had great success creating collisional models of clusters with fully-realized binary dynamics and detailed prescriptions for stellar and binary evolution. It is now routine to create entire grids of N -body star cluster models with $> 10^6$ stars and binaries covering a realistic range of initial conditions that can reproduce GCs and other massive star clusters in the local universe. But while this approach has had great success creating models of individual star clusters in the MW (e.g., van der Marel et al. 1997; Hurley et al. 2001; Baumgardt et al. 2003; Heggie & Giersz 2014; Heggie 2014; Wang et al. 2016a; Kremer et al. 2018; Ye et al. 2021), near every study of Galactic and extra-galactic GC systems has started from idealized grids of initial conditions designed only to reproduce MW GCs. While this method allows us to create one-to-one mappings between individual MW clusters and N -body models (e.g., Baumgardt & Hilker 2018; Weatherford et al. 2020; Rui et al. 2021b), it neglects the wealth of information that cosmological models of star cluster formation can provide, such as the cluster initial mass function (CIMF), initial radii, metallicities, ages, galactic tidal fields, and more. While these quantities are critical components of most semi-analytic models of GC evolution, they have never been self-consistently adopted by the GC modeling community.

We have recently developed a new framework for modeling cluster formation in cosmological simulations of galaxy formation and assembly (Grudić et al. 2022, hereafter Paper I). Using a suite of models of cloud collapse and cluster formation (with resolution of ~ 0.1 pc and a detailed treatment of stellar feedback, Grudić et al. 2021), we created a procedure to directly link the properties of self-gravitating and collapsing giant molecular clouds (GMCs) identified in cosmological simulations (using the results of Guszejnov et al. 2020) to the masses, concentrations, and radii of the clusters they eventually form. In Paper I, this framework was applied to a magnetohydrodynamical (MHD) simulation of a galaxy and its cosmological environment created as part of the Feedback In Realistic Environments (FIRE) project¹ (Hopkins et al. 2014; Hopkins 2017). Paper I was focused on the properties of the YMCs, and in this paper we seek to understand what this cluster population looks like at $z = 0$. This requires not only the initial conditions of the cluster population, but a detailed treatment of the internal dynamics and evolution of collisional star clusters and their interaction with their galactic environment after formation.

To that end, we have created the first *evolved representative population* of GCs using fully-collisional, star-by-star N -body models. The initial masses, radii, metallicities, and birth times for these clusters are taken directly from collapsing GMCs across cosmic time in the m12i MHD simulation (with a gas resolution as fine as

1 pc Wetzel et al. 2016; Hopkins et al. 2020), with unique N -body initial conditions generated for each YMC, while the subsequent dynamical evolution is informed by the time-dependent galactic coordinates and applied tidal forces of associated stars in the cosmological simulation. We then integrate these clusters forward in time to $z = 0$ with our Cluster Monte Carlo code (CMC, Joshi et al. 2000; Pattabiraman et al. 2013; Rodríguez et al. 2022). The Hénon method upon which CMC is based allows us to follow the evolution of dense, spherical star clusters with more than 10^7 stars and binaries (far beyond the capabilities of direct-summation N -body codes), enabling star-by-star simulations of the largest clusters in the m12i galaxy. Furthermore, by tracing the time-dependent tidal forces extracted from the galactic potential, we calculate the tidal boundary of each cluster along its trajectory in the galaxy, allowing us to study the relationship between the clusters' initial conditions, internal evolution, and the galactic environment they reside in. This means that we can accurately simulate the most relevant physical processes for the long-term evolution and survival of YMCs as they mature into GCs.

In §2, we describe the details of our cluster N -body simulations, how we generate initial stellar profiles from the results of the Paper I catalog, and how the influence of the galactic environment (e.g. tidal forces and dynamical friction) is modeled in CMC. As a result of the cosmological environment, a significant fraction of our clusters are shown to overflow their tidal boundaries at formation, which we analyze in detail §3. In §4, we compare the properties of the clusters that survive to the present day ($z = 0$) to the masses, metallicities, ages, and radii of GCs in the MW and M31. Defining GCs as clusters older than 6 Gyr, we find that we can largely reproduce the correct number of MW GCs; however, our GCs are typically younger, less massive, and more core collapsed than those in the MW. In §5, we argue that this discrepancy is due to a complex interplay between the typical tidal fields experienced by clusters formed at different times, and the accelerated core collapse experienced by higher-metallicity (younger) clusters. We also show that our model produces GCs that inhabit roughly the same mass-radius space as other models of long-term cluster survival in the MW (e.g. Gnedin & Ostriker 1997), and compare our results to other studies of star cluster evolution in cosmological simulations, namely the E-MOSAICS simulations of Pfeffer et al. (2018) and the ART simulations of Li et al. (2017).

2 CLUSTER INITIAL CONDITIONS AND COSMOLOGICAL EVOLUTION

The grids of initial conditions to attempt to reproduce the wide range of GCs observed in the MW (e.g. Morscher et al. 2015; Belloni et al. 2016; Rodríguez et al. 2018a; Kremer et al. 2020a; Maliszewski et al. 2021) typically cover a wide range of initial star cluster masses and virial radii (defined as $r_v = -\frac{GM^2}{4E}$, where E is the total kinetic and potential energy of the cluster). Star clusters characteristic of MW GCs are challenging to evolve — even a GC with a present-day mass of $2 \times 10^5 M_\odot$, near the median of the MW GC mass function (GCMF, Harris 2010) must be initialized with $N \sim 8 \times 10^5$ particles, and an virial radius of 1 – 2 pc, beyond what direct N -body integrators can accomplish in a reasonable time frame, to say nothing of the compact radii required to model core-collapsed GCs (Kremer et al. 2019) or GCs with present-day masses of $\gtrsim 10^6 M_\odot$ (e.g. 47 Tuc, Giersz & Heggie 2011; Ye et al. 2021). Instead, studies of these largest clusters have relied upon approximate techniques, such as the Monte Carlo approach

¹ See <http://fire.northwestern.edu>

introduced by Hénon (1971a,b). The two most recent Monte Carlo parameter sweeps (Kremer et al. 2020a; Maliszewski et al. 2021) have used grids of initial conditions covering a range of masses, virial radii, metallicities, and fixed tidal fields. The stellar positions and velocities are sampled from a King (1966) profile and evolved dynamically for approximately one Hubble time. Both these studies have shown that they can largely cover the observed range of GCs and other massive star clusters observed in the MW and beyond.

But while these grid-based studies have demonstrated much success over the years, following an entire population of YMCs from formation in their galactic environments would offer a better understanding of the present-day GC population, act as a powerful probe of the process of GC formation itself (particularly given the unique tidal forces experienced by clusters during different epochs of star formation in galaxies), and may even place constraints on galaxy formation models based on the observed properties of present-day GCs. To that end, we make several modifications to the traditional grid-based initial conditions used by Monte Carlo N -body studies: first, we use a subset of the catalog from Paper I as our initial conditions. These initial conditions cover a wide range of initial masses, radii, metallicities, and formation times. We evolve each cluster forward from its birth time in the FIRE-2 m12i galaxy to either the present day, or its dynamical destruction. Second, our initial cluster models are generated using Elson, Fall and Freeman density profiles (EFF, Elson et al. 1987) rather than the traditional King or Plummer profiles (which assume the clusters to already be in tidal equilibrium with their surrounding environments). Third, the tidal boundary of each cluster is set by the galactic potential of the m12i galaxy, allowing us to resolve the effects of a realistic galactic evolutionary history on a population of YMCs. We now discuss the details of our Monte Carlo N -body approach, and how each of these new physical processes are incorporated into the CMC-FIRE GC systems and their respective assumptions and limitations.

2.1 The Cluster Monte Carlo code, CMC

The N -body models presented here were generated with CMC, a Hénon-style Monte Carlo approach to collisional stellar dynamics (Joshi et al. 2000; Pattabiraman et al. 2013; Rodriguez et al. 2022). Unlike traditional N -body integrators, where the accelerations are calculated by directly summing pairwise gravitational forces, CMC assumes that for sufficiently large clusters, the cumulative effect of many two-body encounters can be understood as a statistical process. Here, “sufficiently large” refers to the Fokker-Planck regime, where the relaxation timescale of any particle (that is, the time for its velocity to change by order of itself) is much longer than the orbital timescale of the particle in the cluster. In this regime, the diffusion of energy and angular momentum between particles can be modeled via *effective encounters* between neighboring particles, where the deflection angle of the encounter is chosen to reproduce the cumulative effect of many distant two-body encounters. This approach has been shown many times to reproduce the pre- and post-core collapse evolution of dense spherical star clusters when compared to both direct N -body simulations and theoretical calculations (e.g., Aarseth et al. 1974; Joshi et al. 2000; Giersz et al. 2013; Rodriguez et al. 2016b; Rodriguez et al. 2022).

CMC relies on pairwise interactions between neighboring stars and binaries to model the effect of many weak two-body encounters. But this scheme allows us to model strong interactions—close encounters where additional stellar and binary physics comes into play—just as easily. These include chaotic encounters between single and binary stars, integrated directly with the *fewbody* small- N body

code (Fregeau & Rasio 2007), direct physical collisions, and binary formation through either the Newtonian interaction of three unbound stars (Morscher et al. 2013), or two-body captures facilitated by tidal dissipation (Ye et al. 2021) or gravitational-wave emission (Rodriguez et al. 2018b; Samsing et al. 2020). Each dynamical timestep allows energy and angular momentum to be exchanged between neighboring particles, pushing the stars and binaries onto new orbits within the cluster potential. For an isolated cluster, some fraction of these orbits will naturally diffuse to positive total energies, representing the classical *evaporation* of stars from the cluster. For clusters embedded in a host galaxy, the rate of stellar loss is enhanced by the *tidal stripping* of stars by the galactic potential, similar to the overflow of the Roche Lobe in binary stars (e.g., Spitzer 1987; Fukushige & Heggie 2000; Renaud et al. 2011). CMC treats both processes, removing unbound stars and binaries after every timestep (see §2.4 and Appendix B for a description of our implementation of tidal forces in a changing galactic potential).

In addition to the relevant gravitational dynamics, CMC includes metallicity-dependent prescriptions for the evolution of stars and binaries using the Binary Stellar Evolution (BSE) package of Hurley et al. (2000, 2002). CMC uses the version of BSE that has been upgraded as part of the COSMIC population synthesis code (Breivik et al. 2020). The version of COSMIC employed here (v3.3) includes new prescriptions for compact-object formation and supernova (Kiel & Hurley 2009; Fryer et al. 2012; Rodriguez et al. 2016a), stellar winds (Vink et al. 2001; Belczynski et al. 2010), stable mass transfer (Claeys et al. 2014) and more. See Breivik et al. (2020) for details. Because every star and binary in the cluster has a time-dependent mass, radius, and luminosity in every snapshot, it is also possible to calculate black-body spectra for both individual stars and the cluster as a whole, which can then be combined into a mock observations of the cluster through any number of appropriate filters. See Section §4.

2.2 Initial Dynamical Profiles of Clusters

For old clusters which have dynamically relaxed, one can assume that the cluster has reached a sufficiently steady state that it can be described by an isothermal energy distribution. Of course, in realistic clusters, the presence of a tidal boundary means that the energy distribution must go to zero at some boundary, as is the case with the often employed King (1966) distribution function. But YMCs, which have not had sufficient time to come into equilibrium with their surrounding environments, are neither expected nor observed to follow such trends. In fact, observations suggest that YMCs typically follow extended power-law profiles with no discernible tidal boundary (Elson et al. 1987; Ryon et al. 2015; Grudić et al. 2018; Brown & Gnedin 2021). Following these observations, our clusters are initialized using an EFF profile, which was originally used to fit surface brightness profiles of YMCs in the Magellanic Clouds (Elson et al. 1987), with a 3D density profile given by:

$$\rho(r) = \rho_0 \left(1 + \frac{r^2}{a^2} \right)^{-\frac{\gamma+1}{2}}, \quad (1)$$

where ρ_0 is the central cluster density, a is a scale radius, and γ corresponds to the power-law index of the outer regions of the surface brightness profile. Note that while $\gamma = 4$ corresponds to the well-known Plummer (1911) profile, observations of YMCs are typically better fit with shallower profiles, where $\gamma \sim 2.2 - 3.2$ (e.g., Mackey & Gilmore 2003a,b; Portegies Zwart et al. 2010; Ryon et al. 2015).

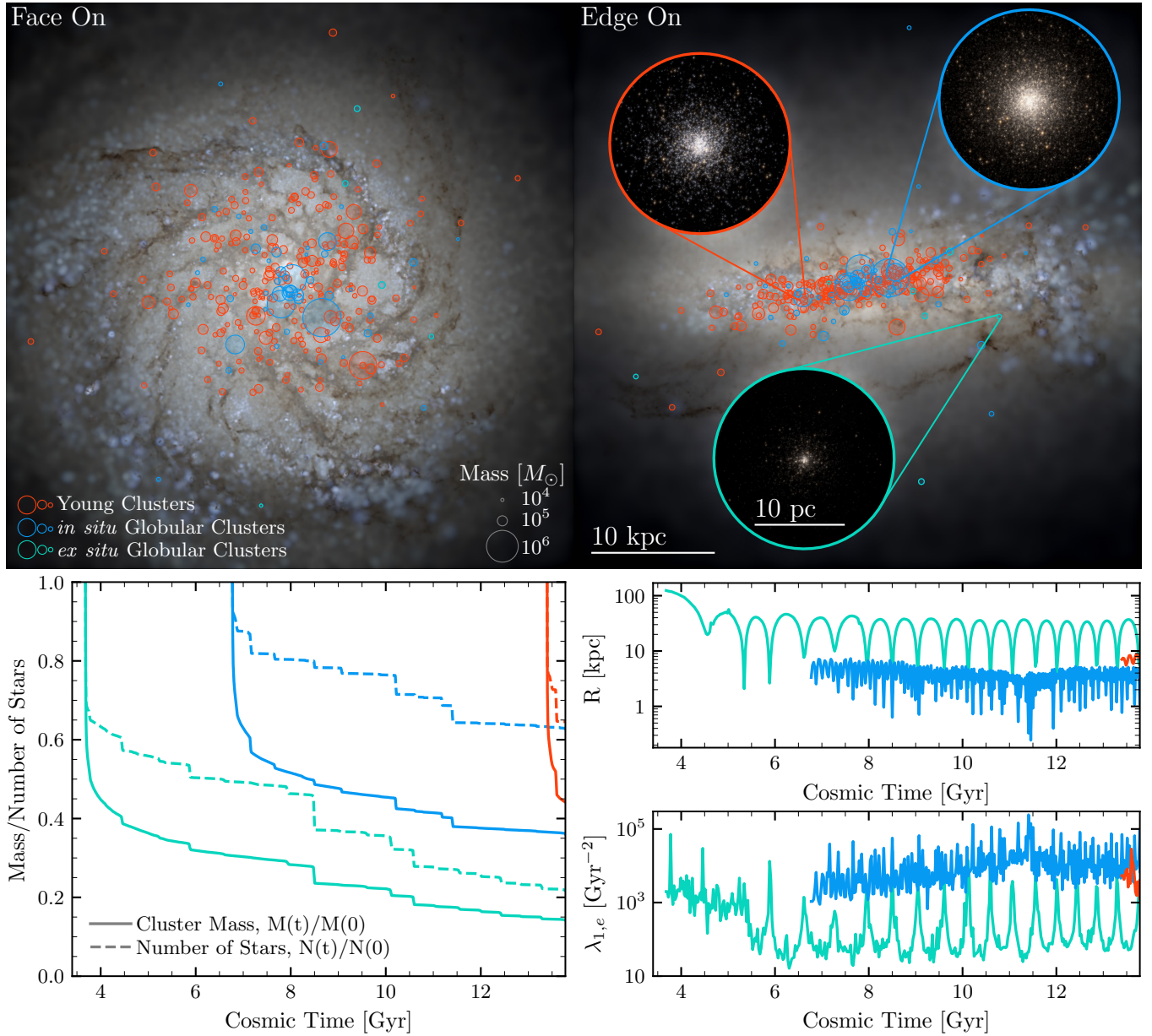


Figure 1. The galactic environment and dynamical evolution of three typical clusters – one formed *in situ*, one formed *ex situ*, and one formed recently – with properties similar to GCs in the MW. We follow each cluster from their births to the present day. The **top** two panels show face-on and edge-on mock HST images (generated using the FIRE Studio, Gurvich 2021) of an MHD FIRE simulation of a MW-mass galaxy (m12i), with the surviving GC population in blue (for clusters born *in situ* in the main galaxy) and green (for clusters born *ex situ* in dwarf galaxies accreted by the main galaxy) while younger clusters are shown in red. Circle size corresponds to present-day cluster mass. We also show three mock HST images typical clusters at $z = 0$ (generated with the Fresco package, Rieder & Pelupessy 2019). The **bottom left** panel shows the mass and the total number of particles in each cluster as a function of galactic cosmic time. The **middle right panel** shows the galactocentric radius of the clusters over their orbits, while the **bottom right panel** shows the effective tidal strengths they experiences over their lifetimes (see §2.4). The sharp decreases in cluster mass are caused by peaks in $\lambda_{1,e}$, as the outer parts of the clusters are stripped away by changing tidal fields as the clusters pass through the disk and near the galactic bulge.

Each cluster in the catalog from Paper I was assigned an initial EFF profile according to the cluster formation model, producing a list of γ parameters and effective radii. To initialize our N -body models, we generate the cumulative mass distribution, $M(r)$, by integrating Equation (1) for a given γ and scale parameter a (chosen to give the correct effective radius), and proceed to randomly sample stellar positions from $M(r)/M(\infty)$. For each star, we also draw a

velocity from the local velocity dispersion given by one of the 1D Jeans equations for spherical systems (following Kroupa 2008):

$$\sigma^2(r) = \frac{1}{\rho(r)} \int_r^\infty \rho(r') \frac{GM(r')}{r'^2} dr' . \quad (2)$$

For each star at a radius r , we compute $\sigma^2(r)$, and draw the individual components of the velocities from a Gaussian distribution

with width σ . This is similar to other codes used to generate N -body initial conditions (Küpper et al. 2011), though we note that this approach does not correctly account for particles in the tail of the velocity distribution with $v > v_{\text{esc}}$, which would be absent in a collisionless equilibrium. However, such particles are expected to be removed from the cluster on an orbital timescale.

Finally, our cluster initial conditions are generated with distributions of star and binary masses and other properties typical for N -body simulations of star clusters. After the particle positions and velocities are sampled, we draw random stellar masses from a Kroupa (2001) initial mass function sampled between 0.08 and $150 M_{\odot}$. Of these stars, 10% are randomly selected to become binaries. The mass ratios of the binaries are drawn from a uniform distribution between 0.1 and 1. The semi-major axes are drawn from a flat-in-log distribution (Duquennoy & Mayor 1991) with a minimum equal to the point of stellar contact for the two stars and a maximum equal to the hard-soft boundary for a binary with those masses at that point in the cluster (out to a maximum of 10^5 AU). Eccentricities are drawn from a thermal distribution ($p(e) \propto e$, Ambartsumian 1937).

2.3 YMC Catalog from Paper I

The complete set of properties that determine our cluster initial conditions (as described in the prior section) are taken directly from the YMC catalog in Paper I. In brief, to generate the catalog we mapped the properties of high-resolution, small-scale simulations of individual GMC collapse onto a full cosmological simulation. The metallicity, mass, surface gas density, and radius of a GMC are used as input to create distributions of star cluster masses and radii (Equations 1-5 and 6, respectively, in Paper I, ²). To create our population, we draw random YMC masses until all of the predicted gas mass in a specific GMC that is to be turned into gravitationally-bound stars has been converted into YMCs. Each cluster is then assigned a half-mass radius following Equation 6 in Paper I and an Elson γ parameter from the universal relation identified in Grudić et al. (2021, Equation 20), while the cluster's stellar metallicity is inherited directly from the gas metallicity of the GMC. The birth times of a cluster is drawn from a uniform distribution over the time interval of the m12i snapshot where their parent GMC was identified. Since most GMCs typically disperse within ~ 3 -10 Myr, and most snapshots were spaced 22 Myr apart, it is likely that many of the GMCs formed in the m12i galaxy were formed in between snapshots. To account for this, we resample the GMC population following the procedure outlined in Paper I, Section 2.3.1.

This initial cluster catalog contains 73,461 entries with masses from $10^4 M_{\odot}$ to $10^7 M_{\odot}$ and covers a wide range of metallicities, ages, galactic positions, sizes, and stellar densities. From this catalog, we restrict ourselves to clusters with initial masses greater than $6 \times 10^4 M_{\odot}$, corresponding roughly to initial particle numbers of 10^5 or greater. This choice was motivated both by our interest in the most massive clusters in the galaxy (the progenitors of GCs), and to ensure that our clusters are sufficiently large for the Hénon method to be reliable.³ This initial cut leaves us with 3165 initial clusters

which, because of limited computational resources, we randomly select 895 for integration⁴.

For computational tractability, we make several modifications to the initial properties of the 895 clusters we present throughout this paper. First, for the sake of computational speed, we truncate the lower limits of our initial virial radii and cluster profile slopes to 0.8 pc and $\gamma = 2.5$ respectively. This was done after testing showed that clusters with very compact radii and very flat mass distributions produce unreasonably high central densities. As an example, our most massive cluster at $5 \times 10^6 M_{\odot}$ would naively yield an initial central density of $\rho_0 \sim 10^{10} M_{\odot}/\text{pc}^3$ with $r_v = 0.8$ pc and $\gamma = 2.01$ (versus $\rho_0 \sim 10^8 M_{\odot}/\text{pc}^3$ when $\gamma = 2.5$). Since even the densest nuclear star clusters observed have inferred central densities of $\sim 10^7 M_{\odot}/\text{pc}^3$ (e.g., Lauer et al. 1998; Schönödel et al. 2018), we elect to truncate our catalog such that all clusters with initial γ values between 2.01 and 2.5 are generated at exactly $\gamma = 2.5$. While the virial radius truncation only affects 17% of clusters, 57% of clusters initially had $\gamma < 2.5$. This artificial truncation means that our evolved cluster population may significantly under-predict the number of stellar mergers and runaway collisions that occur at early times (e.g. Portegies Zwart et al. 2004), thereby underestimating the number of massive black holes formed (e.g., Kremer et al. 2020b; González et al. 2021). However, because our cluster population also has higher stellar metallicities than the aforementioned studies, any massive stellar merger products are greatly reduced by stellar winds; for example, the aforementioned massive cluster undergoes a runaway stellar merger, producing a $\sim 1000 M_{\odot}$ star. But the strong stellar winds driven by higher stellar metallicities reduce the star's mass by nearly 90%, yielding a black hole with mass $< 100 M_{\odot}$. We also truncate the upper metallicity of the clusters to $1.5 Z_{\odot}$ (effecting 15% of the catalog), since our stellar evolution prescriptions are not valid above this metallicity in the original models presented in Hurley et al. (2000). Second, an error was discovered between our initial development of the catalog in Paper I and the current published version in Grudić et al. (2021) which caused incorrect metallicities to be used when determining the distribution of initial radii for the clusters we evolve here. While our distribution of half-mass radii only depends very weakly on metallicity ($r_h \propto \left(\frac{Z_{\text{GMC}}}{Z_{\odot}}\right)^{1/10}$, see Equation 6 of Paper I), this error causes our initial half-mass radii to be at most ~ 1.5 times smaller (in the worst case) than the actual catalog presented in Paper I (where the error was corrected). Due to computational requirements, it is prohibitive to rerun the entire catalog, so instead we assign to each cluster a weight defined by the ratio of the probability of a given cluster radius in the correct distribution to the probability of that radius in distribution it was drawn from (i.e., $w = p_{\text{correct}}(r_v)/p_{\text{original}}(r_v)$). These weights serve to essentially resample our results presented here according to the correct catalog distributions. The distribution of the weights themselves (i.e. how much correction is required) has a median of 0.92, with 90% of weights lying between 0.44 and 1.94, suggesting that our initial cluster population is not substantially effected by this discrepancy. Finally, because we have only selected 895 of the total 3165 clusters with $> 6 \times 10^4 M_{\odot}$, we also multiply each of these weights an additional factor of 3.54; these weights are then used

² See also Grudić et al. (2021, Sections 3.4-3.6) where these distributions were originally developed using specialized high-resolution MHD simulations of collapsing GMCs.

³ As stated in §2.1, the Hénon method formally requires a sufficiently large number of particles to ensure that the relaxation time of the cluster is significantly longer than the typical dynamical time (i.e. $T_{\text{dyn}} \ll T_{\text{relax}}$). Previous work (Freitag 2008) has suggested that this criterion is satisfied

when $N \gtrsim 3000 m_{\text{max}}/\langle m \rangle$, which for an average mass of $\langle m \rangle \approx 0.6 M_{\odot}$ and a maximum mass of $m_{\text{max}} \sim 40 M_{\odot}$ (the maximum BH mass after the first few Myr of stellar evolution), gives a minimum reliable initial particle number of $\sim 10^5$, corresponding to a minimum mass of $\sim 6 \times 10^4 M_{\odot}$.

⁴ Even then, our cluster catalog required $\gtrsim 2$ million CPU hours to evolve, nearly twice as many as the MHD m12i galaxy itself!

to compute all of the distributions and fractions we quote here, but note that this weighting is *not* applied to scatter plots.

2.4 Mass Loss from Time-Varying Galactic Tidal Fields

As previously described, all star clusters will slowly shed their stars, either through natural evaporation at the high energy tail of the stellar distribution function, or through tidal stripping by the tidal fields of the cluster’s host galaxy. While these are often presented as separate processes, the mechanism is largely the same: stars still diffuse towards positive energies due to two-body relaxation, but in the presence of a galactic tidal field, the threshold for positive energy is decreased from 0 to some E_t which defines the Jacobi surface. The only difference is that in the case of the tidal field, this zero energy surface is not spherically symmetric about the cluster, making it easier for a particle to escape in certain directions (e.g. the L1 and L2 Lagrange points). In general, the location of this boundary can be identified as the point where the acceleration from the cluster potential cancels that of the galactic tidal field:

$$\frac{d^2\mathbf{r}'}{dt^2} = -\nabla\phi_c(\mathbf{r}') + \mathbf{T}(\mathbf{r}') \cdot \mathbf{r}' \quad (3)$$

where ϕ_c is the gravitational potential of the cluster and \mathbf{T} is the tidal tensor of the galactic potential ϕ_G at the point \mathbf{r}' , defined as

$$\mathbf{T}^{ij} \equiv -\left(\frac{\partial^2\phi_G}{\partial x^i\partial x^j}\right)_{\mathbf{r}'} \quad (4)$$

Equation (3) describes the forces experienced by a star in the cluster in the rest frame of the galaxy. However, what we are interested in is the force in the rest frame of the cluster. This transformation to a rotating reference frame naturally introduces additional pseudo-forces (Coriolis, centrifugal, etc.) that depend on both the orbit of the cluster in the galaxy and the 3D structure of the cluster with respect to the galactic orbit; see, e.g., [Renaud et al. \(2011\)](#). Because CMC assumes clusters to be spherical anyway, we only need the spherical average of the cluster tidal boundary. We use the prescription from Appendix C of [Pfeffer et al. \(2018\)](#), and define the *effective* tidal strength as $\lambda_{1,e} \equiv \lambda_1 - 0.5(\lambda_2 + \lambda_3)$, where $\lambda_{1,2,3}$ are the Eigenvalues of the tidal tensor (Equation 4) sorted from largest to smallest. Diagonalizing the tidal tensor transforms it into the rotating frame of the cluster, where λ_1 is the gravitational force along the vector pointing from the cluster center to the galactic center, and $0.5(\lambda_2 + \lambda_3) = \Omega^2$ is the centrifugal force of a circular orbit in a spherical potential (in a true spherical potential $\lambda_1 = \lambda_2 = \Omega^2$, see [Pfeffer et al. 2018](#), Appendix C). The instantaneous tidal radius of the cluster is then given by (e.g., [Renaud et al. 2011](#)):

$$r_t = \left(\frac{GM_c}{\lambda_{1,e}}\right)^{1/3} \quad (5)$$

where M_c is the cluster mass. With Equation (5), we can apply a time-dependent tidal boundary to our CMC clusters, so long as we can calculate $\lambda_{1,e}$.

For each cluster from the [Paper I](#) catalog, we identify a single star particle in the cosmological simulation that was associated with its parent GMC in the m12i galaxy and use it as a tracer particle for the cluster’s trajectory from birth until either $z = 0$ or cluster destruction. With the exception of dynamical friction (discussed momentarily), the trajectory of the clusters is fully-resolved by the cosmological simulation — the tracer particles have a mass

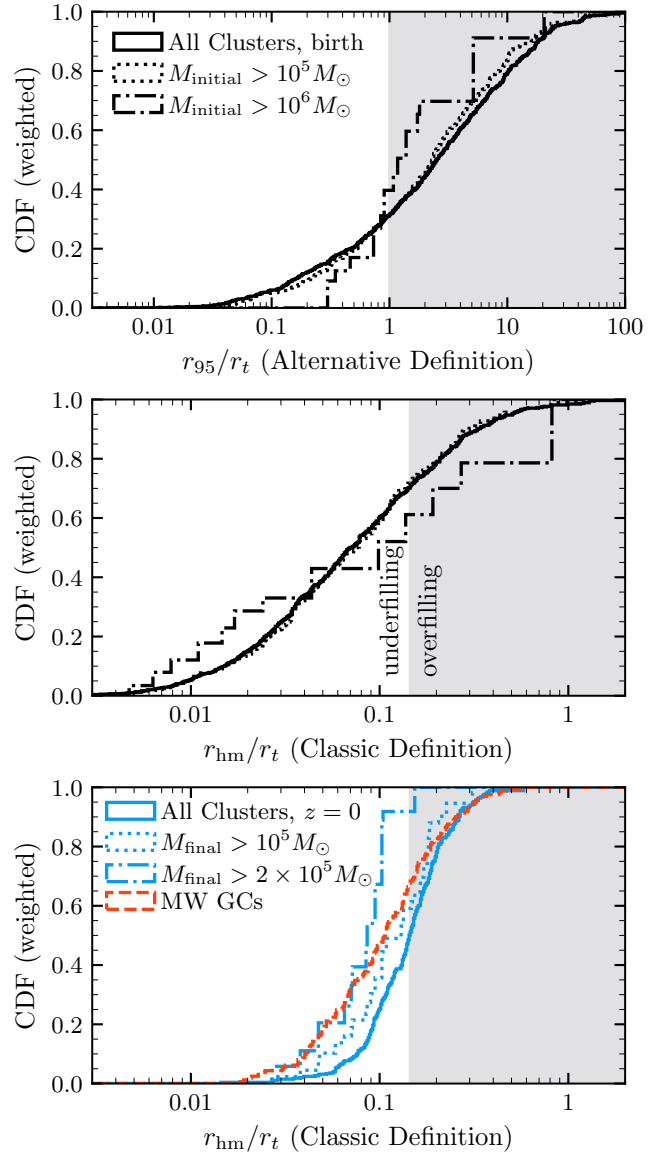


Figure 2. The tidal filling of the cluster population both at birth and at $z = 0$ in the m12i galaxy. In the **top** panel, we show the cumulative distribution of tidally filling clusters using our alternative definition (where a cluster is overfilling if its 95% Lagrange radius is larger than its initial tidal radius) at birth across all redshifts, across all clusters (solid line) and for clusters with masses greater than $10^5 M_\odot$ and $10^6 M_\odot$ in dotted and dashed-dotted, respectively. Note that this definition (which is more appropriate for the EFF profiles our clusters are initially sampled from) suggests that nearly 70% of clusters in our catalog are initially overflowing their tidal boundaries. In the **middle** panel, we show the same distribution using the classic definition of tidal overfilling, $r_{\text{hm}}/r_t > 0.145$ (following [Hénon 1961](#)), where r_{hm} and r_t are the half-mass and tidal radii of the clusters, respectively. In the **bottom** panel, we show the same quantity, but for those clusters that survive to $z = 0$. We also show the distribution of r_{hm}/r_t for MW GCs from the catalog assembled in [Baumgardt \(2017\)](#); [Baumgardt & Hilker \(2018\)](#); [Vasiliev & Baumgardt \(2021\)](#). The cumulative distributions are weighted following the discussion in §2.3. The gray shaded regions in each plot indicate where clusters are overfilling, according to given definition.

resolution of $\approx 7 \times 10^3 M_\odot$ compared to the cluster mass range of $10^4 - 10^7 M_\odot$. We then extract from every m12i snapshot⁵ the second derivatives of the local galactic potential (Equation 4; the potential itself is stored in the simulation output) about that star particle, as well as the local position, velocity, enclosed galactic mass, and local velocity dispersion at that point in the m12i galaxy (used in computing the dynamical friction timescale described below). This procedure is similar to that we used for *Behemoth*, the largest cluster from this catalog (previously described in Rodriguez et al. 2020). We show an example of the position and tidal forces experienced by typical clusters (that survives to $z = 0$) in Fig. 1. Once we have extracted the tidal tensor, it is passed as input to CMC, which then diagonalizes the tidal tensor and linearly extrapolates in time the value of $\lambda_{1,e}$ between the snapshots of the m12i model. The instantaneous tidal boundary is computed using Equation (5). Each timestep, CMC strips any star whose orbital apocenter is greater than r_t . Note that this is different from previous CMC models and other Monte Carlo codes (e.g. Giersz et al. 2008), which used a stripping criterion based on the potential energy of the cluster at r_t ; however, we have found that our choice better replicates the mass-loss rates for star clusters on eccentric orbits (see Appendix A). Because the galactic potential (and therefore the tidal tensor) is calculated on the same scale as the typical inter-particle separation (~ 6.5 pc for this simulation; see Hopkins et al. 2018, §4.2), we are able to resolve nearly all relevant physical structures that can significantly influence the tidal field of our GCs.

While our approach allows us to model the effect of arbitrary tidal fields on our GC models, what it does *not* capture is the affect on the cluster’s orbit in the galaxy due to dynamical friction. Of course, these two effects are not independent: as dynamical friction shrinks the orbit, the tidal fields tend to become stronger toward the denser galactic center. In turn, stronger tidal fields strip more stars, causing the cluster to lose mass and dynamical friction to become less efficient. These effects are particularly difficult to model within gravitationally-softened cosmological simulations, where the star particles we use to trace the clusters’ orbits have similar masses to other particles (see e.g., Tremmel et al. 2015; Ma et al. 2021, for similar issues relating to supermassive BHs).

While we cannot self-consistently calculate new cluster orbits in the cosmological simulation during a CMC integration, we can calculate the time it would take for dynamical friction to drive our clusters into the galactic center (again following Pfeffer et al. 2018). We use the dynamical friction timescale from Lacey & Cole (1993):

$$T_{\text{df}} = \frac{\epsilon^{0.78}}{2B(v_c/\sqrt{2}\sigma)} \frac{\sqrt{2}\sigma r_{\text{circ}}^2}{GM_c \log \Lambda}, \quad (6)$$

where r_{circ} is the radius of a circular orbit with the same energy E as the actual test particle, v_c is the circular velocity at that radius, M_c is the cluster mass, $B(x) = \text{erf}(x) - 2x \exp(-x^2)/\sqrt{\pi}$ is the standard velocity term for dynamical friction (Binney & Tremaine 2008), ϵ is the ratio of the angular momentum of the real orbit to that of the circular orbit at r_c (to correct for the effects of eccentricity, Lacey & Cole 1993), and $\log \Lambda$ is the Coulomb logarithm, defined here as $\Lambda = 1 + M_c/M_{\text{enc}}$ for an enclosed mass M_{enc} . We pass as input to CMC the cluster’s position, velocity, enclosed galactic mass, and local velocity dispersion, and calculate Equation (6) every timestep.

⁵ With the exception of the *first* m12i snapshot, which still contains the tidal contribution of the cluster’s birth GMC. In practice, we use the tidal tensor from the second snapshot for both initial

Because T_{df} can change dramatically over a single cluster orbit, we integrate each cluster until a single T_{df} has elapsed:

$$\int \frac{dt}{T_{\text{df}}} > 1, \quad (7)$$

using the same orbits extracted in the previous section. Once (7) is satisfied, we assume the cluster has been destroyed. Note that this is different than the approach used in Pfeffer et al. (2018), where a cluster is assumed to have spiraled into the galactic center when its age is greater than T_{df} . We explore the implications of Equation (7) in §5.3.

Finally, we do not include any prescription for the work done by the time-dependent tidal field on cluster itself. This periodic injection of energy, known as *tidal shocking*, has been argued to have significantly shaped the evolution of the cluster mass function in the MW and other galaxies, particularly for clusters with lower masses and larger radii (e.g., Spitzer 1958; Ostriker et al. 1972; Spitzer 1987). This process is particularly difficult to implement successfully in a Monte Carlo code such as CMC, where the assumptions of spherical symmetry, virial equilibrium, and a timestep that is a fraction of the cluster’s relaxation time explicitly preclude including processes that occur on a dynamical timescale or require the 3D positions and velocities of the stars (though see Sollima & Mastrobuono Battisti 2014). However, we can estimate the effect that tidal shocking would have had on the mass-loss rate of our clusters using a similar technique to Pfeffer et al. (2018). We do so in Appendix B, and find that $> 99\%$ of our clusters we estimate to be destroyed by tidal shocking are already destroyed by time-dependent mass loss from tidal stripping.

3 INITIAL CLUSTER POPULATION

It is interesting to compare the tidal truncation of our cluster catalog to the tidal radii and truncation of clusters in the MW. The cluster formation model from Paper I contains no explicit information about the local tidal field where the clusters form external to the progenitor cloud, since the cloud collapse simulations from Grudić et al. (2021) were performed in isolation. As a result, star clusters in our model can occasionally be tidally overfilling immediately after formation, which does represent a significant departure from previous N -body studies of star clusters, where clusters are assumed to be (sometimes significantly) tidally underfilling at birth. This is largely based on the argument that any tidally limited clusters we see today will have expanded over time to fill their Jacobi radii, and for clusters born filling their tidal boundaries, this early phase of expansion would likely lead to rapid destruction by the galactic tidal field (Gieles et al. 2011). This argument has also been used to argue *against* clusters being born with a significant degree of primordial mass segregation (Baumgardt et al. 2008; Vesperini et al. 2009), since such segregation would only increase the cluster expansion during this early phase.

In Fig. 2, we show the cumulative fraction of clusters that are tidally filling at birth and at $z = 0$. Following Hénon (1961) we define tidally overfilling clusters as those where the ratio of the half-mass to tidal radii, r_{hm}/r_t , is greater than 0.145, with r_t defined as the location of the outermost star in the cluster. Using this definition, approximately 25% of our initial cluster population is tidally overfilling at birth. There is also a weak trend of the most massive clusters being more overfilling, with $\sim 40\%$ of clusters with initial masses $> 10^6 M_\odot$ overfilling their tidal boundaries initially.

However, we note that the value of 0.145 is taken from the equal-mass homological model presented in Hénon (1961), and while we have used it here to make it easier to compare our results to the pre-existing literature, there is no reason that this value should apply to the non-equilibrium EFF profiles with realistic stellar mass distributions. A more straightforward statistic would be the ratio of an outer Lagrange radius enclosing some large fraction of the total mass to the tidal boundary. We show the cumulative distribution of r_{95}/r_t , where r_{95} is the radius enclosing 95% of the mass, in the top-right panel of Fig. 2. Here, the situation is reversed: nearly 70% of our clusters have $r_{95} > r_t$ initially, suggesting that the EFF profile generates more tidally overfilling clusters than predicted using the statistic taken from equal-mass homologueous models. Furthermore, the more massive clusters tend to be *less* overfilling under this definition than their lower-mass counterparts.

Observations of YMCs in the 31 galaxies of the Legacy Extragalactic UV Survey suggest a typical mass-radius relationship of the form $r_{\text{hm}} \propto M_{\text{cl}}^{1/4}$ (Brown & Gnedin 2021), though with significant variation in the slopes between different galaxies (G. Brown, private comm.). But the cluster tidal radii scale as $M_{\text{cl}}^{1/3}$ (Equation 5), which would suggest that, all other things being equal, the cluster filling fraction should very weakly ($r_{\text{hm}}/r_t \propto M_{\text{cl}}^{-1/12}$) depend on mass, with more massive clusters being very slightly more likely to overfill their tidal boundaries at birth. This is seen in the top two panels of Fig. 2, where that the dependency of r_{hm}/r_t on mass is weak, but not consistent between the classic and alternative definitions of tidal filling. This is also consistent with the initial cluster catalog from Paper I, which exhibits a $r_{\text{hm}} \propto M_{\text{cl}}^{1/4}$ scaling (Fig. 10; Grudić et al. 2021, Section 3.3) globally, but with significant variation when binned by to the local gas surface density where each cluster was formed. When considering clusters born in environments with similar gas densities, the mass-radius relations follow the $M_{\text{cl}}^{1/3}$ scaling expected for clusters forming at constant density (albeit with different multiplicative coefficients), leaving r_{hm}/r_t with no dependence on cluster mass. It is only after stacking these bins together that the global mass-radius relation follows the aforementioned $M_{\text{cl}}^{1/4}$ scaling. From this, we conclude that the initial fraction of clusters that are overfilling is largely the result of the local galactic environment at formation, rather than any global trend in cluster formation.

In the bottom panel of Fig. 2, we show the distribution of surviving clusters that are tidally filling at the $z = 0$ snapshot of the larger simulation (limiting ourselves to the classic r_{hm}/r_t definition for easier comparison to observations). Here, we find that the distribution of clusters is exactly centered at 0.145, as one would expect for a population of clusters that is both dynamically evolved (i.e. closer to the original homologueous model of Hénon) and in equilibrium with their surrounding environments. We also compare our results to the MW GCs, using the tidal boundaries and half-mass radii from the catalog assembled in Baumgardt & Hilker (2018); Vasiliev & Baumgardt (2021), which rely on a scaled grid of direct N -body models described in Baumgardt (2017) and define r_t using Equation 8 of Webb et al. (2013). Somewhat surprisingly, the distribution of MW GCs appears to be more tidally underfilling than the catalog clusters at $z = 0$ (with only $\sim 1/3$ of the MW clusters overfilling their tidal boundaries). However, we note that measurements of cluster tidal boundaries are extremely difficult; even the N -body models used by Baumgardt (2017) to compare to the MW GCs were performed in isolation, making it difficult to uniquely identify a tidal boundary by comparison to N -body models. Furthermore, while the overall population of cluster models at $z = 0$ seems to diverge from the MW distribution, we note that the cluster

models with final masses $> 10^5 M_{\odot}$ appear more consistent with the MW distribution, while clusters with final masses $> 2 \times 10^5 M_{\odot}$ appear to match very well (for low r_{hm}/r_t values) with the MW population, suggesting that any disagreement may actually be the result of our lower-mass GCMF.

4 PRESENT-DAY CLUSTER PROPERTIES

In addition to masses and other global properties, our star-by-star N -body models allow us to compare the present-day structural parameters of our clusters to those in the MW and M31 as well. In order to create as honest a comparison as possible, we generate for every cluster that survives to the present day an orbit-smoothed synthetic surface brightness profile (SBP) using the `cmctoolkit` (Rui et al. 2021a,b). Each SBP is generated by binning the cluster into 80 logarithmic bins of projected radii between 0.01 pc and the outermost star in the (projected) cluster profile, then applying a generic Johnson V-band filter to the cumulative light emitted in each bin (assuming each star to have a blackbody spectra). GC and YMC observations typically apply magnitude cuts when creating SBPs, to ensure that the profiles are robust tracers of the underlying cluster structure, and to remove any saturated stars from the observation (this is particularly important for younger clusters, e.g., Elson et al. 1989; Mackey & Gilmore 2003a). We apply a similar cut in luminosity by removing any star from our SBPs that contributes more than 0.5% of the total luminosity of the cluster. For most clusters, this typically cuts much less than 1% of the stars (the exception being very small clusters which are near dissolution, for which SBPs would be extremely noisy anyway). Throughout this paper, we distinguish between the half-light radius, r_{hl} , which is the projected 2D radius enclosing half the visual luminosity, and the half-mass radius r_{hm} , which is the 3D radius enclosing half the mass. To calculate other structural parameters, such as the core radius, r_c , and the concentration parameter (defined as $c = \log_{10}(r_t/r_c)$, where r_t is the tidal boundary), we fit each SBP to a projected King (1966) profile. The r_c and r_t parameters are taken directly from these fits (including the aforementioned luminosity cuts).

We also compile a series of observational catalogs to compare our results to. For the masses of the MW GC systems, we use the V-band magnitudes from the Harris (1996, 2010 Edition) catalog and convert them to masses assuming a mass-to-light ratio of 2 for old stellar systems (Bell et al. 2003). The metallicities, core radii, half-light radii, and King concentrations c are also taken from the Harris catalog. For the ages of the MW clusters, we use the 96 cluster ages compiled by Kruijssen et al. (2019) from the surveys presented in Forbes & Bridges (2010); Dotter et al. (2010, 2011); VandenBerg et al. (2013). For the M31 GCs, we take the masses, ages, and metallicities from the Caldwell et al. (2011) catalog, while the King concentrations, core, and half-light radii are taken from the Peacock et al. (2010) catalog. Note that the core radii are not present in the latter, but we calculate them using the provided tidal radii and King concentration parameters.

Finally we must address what we actually define as a “globular” cluster. While our cluster catalog is generated from initial conditions for massive spherical star clusters, they are not uniquely the old, low-metallicity clusters that we typically call “globular” clusters. As stated in Paper I, this galaxy does not produce massive star clusters sufficiently early ($z \gtrsim 3$) to reproduce the classical GCs of the MW. Observed in another galaxy, many of our clusters would instead be identified as open clusters or super star clusters. By limiting our comparison to the old clusters of the MW and M31,

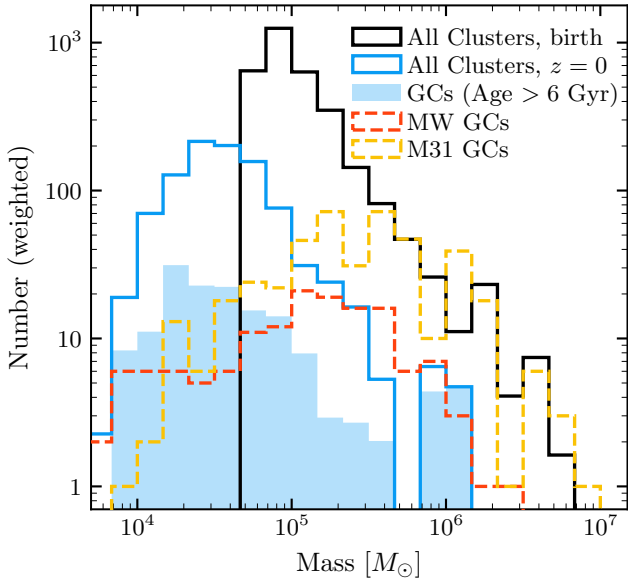


Figure 3. The globular cluster mass function of our CMC-FIRE cluster system. In black, we show the distribution of birth masses of our 895 clusters (across all formation redshifts), while in blue we show the population of clusters that survive to the present day. Both distributions are weighted according to the description in §2.3. We also show the masses of clusters older than 6 Gyr, which we term classical GCs, in solid blue. For comparison, we show the masses of GCs in the MW (Harris 1996, 2010 Edition) and M31 (Caldwell et al. 2011) in dashed red and yellow respectively.

we are largely ignoring the contribution of lower-mass clusters (for which complete catalogs are harder to assemble). Following previous studies (e.g. the E-MOSAICS simulation Pfeffer et al. 2018), and using the youngest GC age in M31 as a guide, we define any cluster formed more than 6 Gyr ago as a GC, while referring to clusters formed less than 6 Gyr ago as young clusters. Finally, we restrict ourselves to clusters that lie within the main MW-like galaxy of the FIRE-2 simulation, which we define to be those within 100 kpc of the galactic center at $z = 0$.

4.1 Cluster Mass Functions

There are multiple physical effects, both internal physical processes and external galactic influences, that determine the evolution of the CMF over cosmic time. Immediately after formation, clusters lose a significant amount of mass through the evolution of massive stars. For our choice of IMF and median cluster metallicity ($\sim 0.6Z_{\odot}$), nearly 20% of the stellar mass is lost to winds and supernova within the first 50 Myr of evolution. This mass loss causes the cluster to expand as it becomes less gravitationally bound. For tidally filling clusters, this means that the outer regions of the cluster can suddenly find themselves beyond the tidal boundary, where they are stripped away by the galactic tidal field. For the typical GCs shown in Fig. 1, the combination of mass loss and stripping conspire to decrease the cluster mass by nearly a factor of two within the first 50 Myr!

After this initial phase of rapid evolution is complete, a typical star cluster begins a slow evolutionary phase, where mass loss is primarily driven by two-body relaxation in the forms of evaporation and tidal stripping. In Fig. 3, we show the evolution of the CMF from birth to the present day, where the physical processes described in §2.4 conspire to shape our $z = 0$ mass function. Limiting ourselves

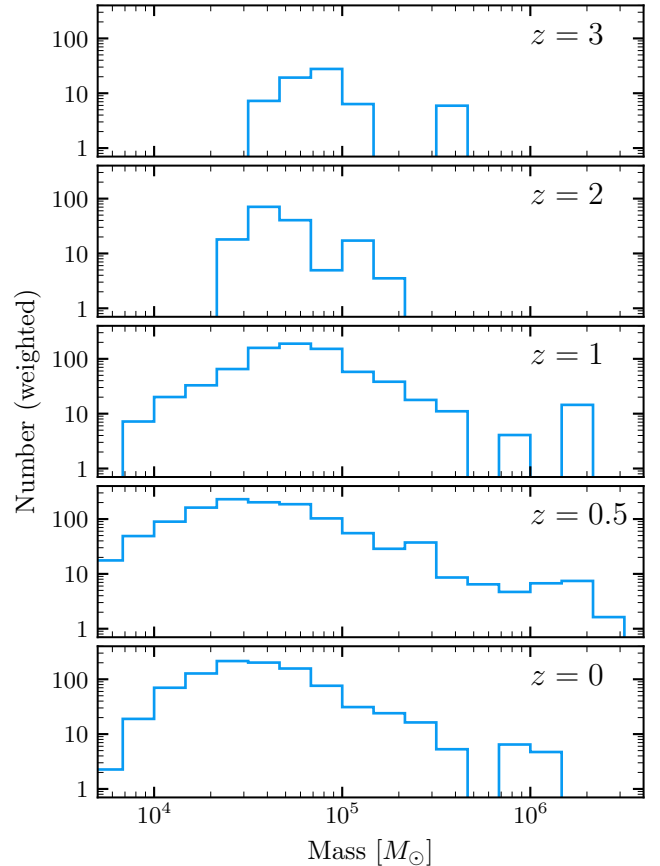


Figure 4. The CMF of our CMC-FIRE cluster system in the main m12i galaxy at various redshifts. Note that this includes all clusters, not just classic GCs.

to those clusters older than 6 Gyr, it is immediately obvious that our $z = 0$ CMF does not match that of either the MW or M31 GCs in the low-mass range, as our catalog contains significantly more clusters with $M \lesssim 10^5 M_{\odot}$. The median of our GCMF is at $\sim 3 \times 10^4 M_{\odot}$, significantly lower than the $\sim 10^5 M_{\odot}$ median of the MW GCs. At the same time, the CMC-FIRE catalog shows good agreement for the numbers of the most massive ($\sim 10^6 M_{\odot}$) GCs, as well as the number of clusters around the median of the MW GC mass function. Furthermore, the *overall number* of GCs in our (weighted) CMC-FIRE catalog is 148, astonishingly close to the actual number of GCs in the MW (157, Harris 1996, catalog, 2010 edition). Including the young clusters (those younger than 6 Gyr), the model predicts 941 massive clusters present in the m12i galaxy at the present day.

There are likely two reasons for the discrepancy in our GCMF, the first being the formation time of clusters (even those defined as GCs) within the m12i galaxy. The median age of the surviving GCs in our CMC-FIRE catalog is 7.9 Gyr (versus 2 Gyr for the young clusters), in stark contrast to the ~ 12 Gyr age of GCs in the MW (Kruijssen et al. 2019). This is shown in Fig. 4, where we show the CMF of our cluster population at various redshifts. Although there is some early cluster formation at high redshifts, the majority of clusters are not present until $z \sim 1$. The number of low-mass clusters significantly increases from $z = 1$ to $z = 0.5$, as the massive clusters formed at $z = 1$ lose mass and fill out the lower regions of the mass function. Somewhat counter-intuitively, we will

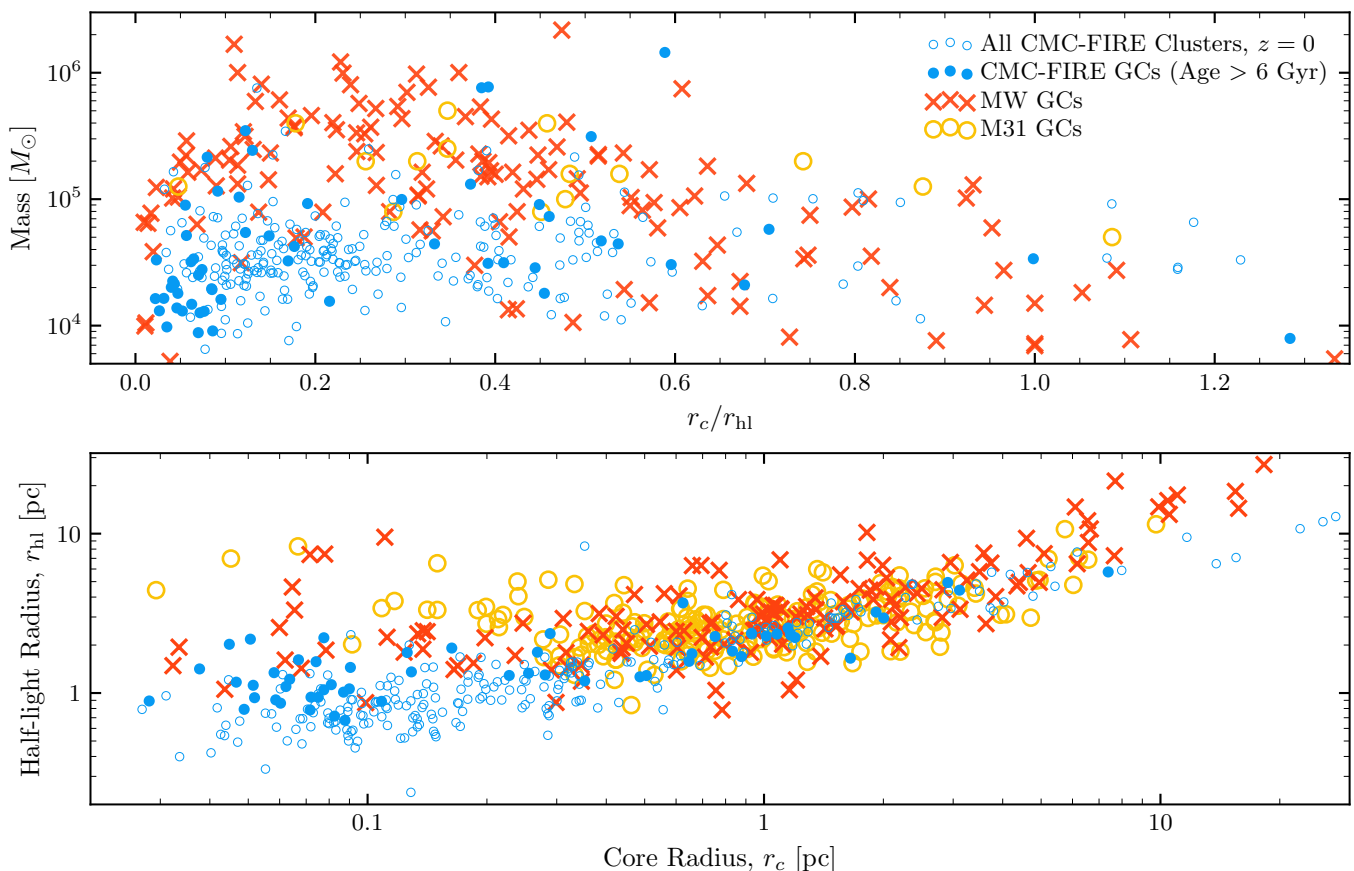


Figure 5. The masses and radii of our surviving 296 (unweighted) cluster models compared to the clusters in the MW and M31. The CMC-FIRE GCs (those older than 6 Gyr) are indicated with blue dots, while younger clusters are indicated with open blue circles. The MW GCs are shown in red x’s (from the [Harris 1996](#), catalog) and the M31 clusters in yellow circles (from the [Peacock et al. 2010](#), catalog); note that the M31 catalog does not contain masses, so we cross reference the entries there with the entries from the [Caldwell et al. \(2011\)](#) catalog (only a handful of clusters appear in both). On the **top**, we show the ratio of the observational core radius r_c to the half-light radius r_{hl} versus the cluster mass. On the **bottom**, we show r_c and r_{hl} separately for all three cluster populations. While in both cases, the CMC-FIRE catalog overpredicts the number of low-mass, compact GCs compared to both the MW and M31 (for the reasons described in Section 4.1), the catalog is largely able to cover the entire range of observed cluster structural parameters.

argue that these clusters lose mass at a rate that is, on average, faster than clusters formed earlier in the galaxy (c.f. Fig. 9, §4.3 and 5.3). This is because, in agreement with previous studies (e.g. [Li & Gnedin 2019](#); [Meng & Gnedin 2022](#)), we find that clusters formed earlier experience weaker tidal fields on average, since they are characteristically formed on wider orbits that are less likely to be aligned with (or lying within) the galactic disk. As we will argue, this is because most GCs are either formed during the early bursty phase of star formation in the main galaxy, when the gas has a quasi-isotropic velocity distribution (e.g., [Gurvich et al. 2022](#), and §4.3), or formed *ex situ* in dwarf galaxies that are accreted by the main galaxy. Because of this, the majority of our old, massive GCs lose more mass and are more likely to be destroyed than had they formed at an earlier epoch.

The second reason for this discrepancy is likely the our prescription for following the effects of tidal shocking on the GC population. As described in Appendix B, we find that *none* of the clusters in our sample of 895 models have been significantly affected by tidal shocking over their evolution. This is largely because the tidal tensors are calculated from the snapshots of a cosmological FIRE simulation, typically spaced every ~ 20 Myr in cosmic time. However, the effectiveness of a tidal shock depends on the amount of

work the tidal field is able to do on the cluster’s dynamical timescale, since otherwise the cluster can undergo slow, adiabatic changes that do not significantly increase the escape rate of stars (though see [Weinberg 1994a,b,c](#), for cases where the injection of energy can be significantly more destructive). Because the median dynamical time of the clusters in our catalog is on the order of ~ 1 Myr, well below the time resolution of tidal forces extracted from the FIRE simulation, none of our cluster would be significantly affected by tidal shocks, even if the physics had been incorporated in CMC. This timestep resolution may be particularly problematic for resolving encounters with GMCs (e.g., [Gieles et al. 2006](#); [Linden et al. 2021](#)) or transits through the galactic disk (e.g., [Ostriker et al. 1972](#)), which may cause significant tidal shocks within a few Myr; see §5.1. This means that we cannot resolve the injection of energy and subsequent expansion of the lowest mass clusters, leaving us with an excess of low-mass GCs compared to the MW or M31. Combined, these two facts conspire to produce a lower median value for our GCMF, despite the agreement between the number of GCs in the MW and m12i.

As for the young clusters, the model prediction of 793 young massive clusters is in stark contrast to the observational picture in the MW, where only $O(10)$ such young clusters are known (e.g.,

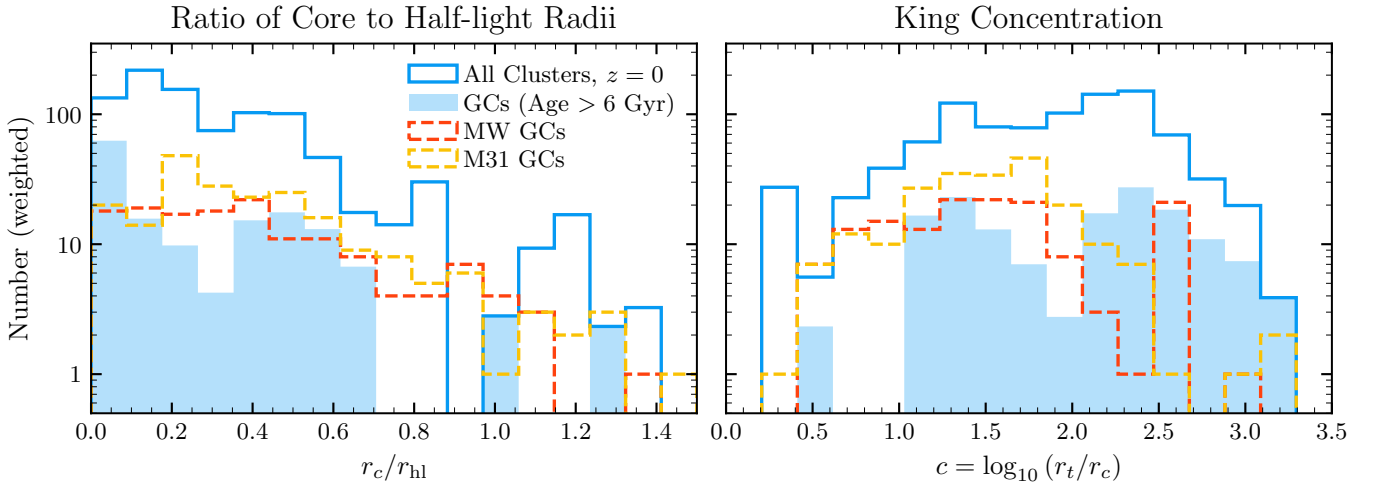


Figure 6. The projected distribution of concentrations for our surviving cluster models (in blue), with the population of old (>6 Gyr) GCs in solid blue, compared to the concentrations of clusters in the MW (in dashed red). On the **left**, we show the distribution of r_c/r_{hl} for both populations (the same as the horizontal axis of the top panel of Fig. 5). On the **right**, we show the histogram of the King concentration parameter, defined as the logarithm of r_t/r_c , where r_t is the tidal radius. The distribution for the MW r_c/r_{hl} and King concentrations are taken from Harris (1996, 2010 edition), while for M31 the distributions for taken from the Peacock et al. (2010) catalog (note that the latter does not contain r_c , so we reconstruct it from the provided values of the King concentration and tidal radii). Finally, note that the peak at $c = 2.5$ in the Harris (1996, 2010 edition) catalog comes from (Trager et al. 1995), where all core collapse clusters are assigned concentrations of exactly 2.5.

Portegies Zwart et al. 2010, Table 2). However, a large part of this disagreement is definitional: restricting ourselves to clusters with ages ≤ 20 Myr and $\geq 10^4 M_\odot$ (as in the previous citation) yields no young clusters at $z = 0$ in the m12i galaxy, while adopting a more loose age cutoff of ≤ 100 Myr yields approximately 6 clusters. What this suggests is that our cluster evolution model overpredicts the presence of *intermediate*-aged massive clusters (between a few 100 Myr and a few Gyr), compared to the MW. However, there are observations of young and intermediate-aged clusters in other galaxies, both within and beyond the Local Group (e.g., Larsen 2010; Richtler et al. 2012), including other spiral galaxies (Larsen & Richtler 1999, 2004). As we describe in §4.3 and 5.1, many of the discrepancies between our m12i galaxy and the MW may arise from the unique assembly history of both systems.

4.2 Cluster Sizes

In Fig. 5, we show the observed radii of our clusters compared to those in the MW and M31. On the top panel, we show the distribution of clusters in mass vs r_c/r_{hl} space (the latter being a proxy for the overall concentration of the cluster). Our CMC-FIRE clusters largely cover the space of MW and M31 clusters, suggesting that our distribution of initial conditions is sufficiently broad to reproduce the range of observed GCs in the local universe. The same is true on the bottom panel of Fig. 5, where we show separately the values of the half-light and core radii. The bulk of clusters in the MW, M31, and m12i galaxies lie along the same relation in r_c/r_{hl} space.

As with the mass distribution, both plots in Fig. 5 show an excess of compact, low-mass clusters in the m12i galaxy as compared to the MW or M31. This likely arises from the aforementioned coarse-grained treatment of tidal shocking and the fact that, counter-intuitively, our younger clusters undergo core collapse faster because of their high stellar metallicities (§5.2). Of course, Fig. 5 only shows the results of our catalog directly, without accounting for our weight-

ing scheme or the fact that we only modeled $\sim 28\%$ of the clusters from the catalog. In Fig. 6, we show the (weighted) distributions of both r_c/r_{hl} and the King concentration parameters. Both the numbers and general shape of the distributions are largely correct for both the r_c/r_{hl} concentration distributions. When considering all cluster ages, the CMC-FIRE system slightly over-predicts the number of clusters with large r_c/r_{hl} ratios. On the other hand, if we restrict ourselves to old, classic GCs, we see significantly fewer clusters with large r_c/r_{hl} or small c values. As we will show in §5.2, this is largely because our clusters have higher stellar metallicities than those in the MW or M31, which in turns drives them to core collapse earlier than their low-metallicity counterparts.

4.3 Ages, Metallicities, and Galactic Positions

Arguably the largest discrepancies between our cluster population and observations is that the majority of our model clusters are significantly younger (and correspondingly higher metallicity) than the old GCs in the MW and M31. This discrepancy is also readily apparent in the ages and metallicities of the clusters that survive to the present day, which we show in Fig. 7. While there exist a handful of GCs with low metallicities ($[Fe/H] \sim -1.6$), similar to the classical “blue” GCs in the MW, the median GC metallicity for the CMC-FIRE catalog is -0.4 , noticeably higher the median of -1.3 in the MW or -0.8 in M31.

This behavior is a direct result of the initial conditions described in Paper I, where the later formation of GCs (compared to those in the MW) is described in detail. What is not immediately obvious is how much of this discrepancy lies in the star-formation history of the m12i galaxy (i.e. whether there is some systematic trend against forming GCs early enough), and how much is simply a byproduct of the inherent galaxy-to-galaxy variation in merger history and cluster formation. It has been shown (e.g., Hafen et al. 2022, Section 4.5) that the star-formation rate of FIRE-2 MW-mass galaxies can be ~ 2 times larger at $3 - 10 M_\odot/\text{yr}$ than observationally-

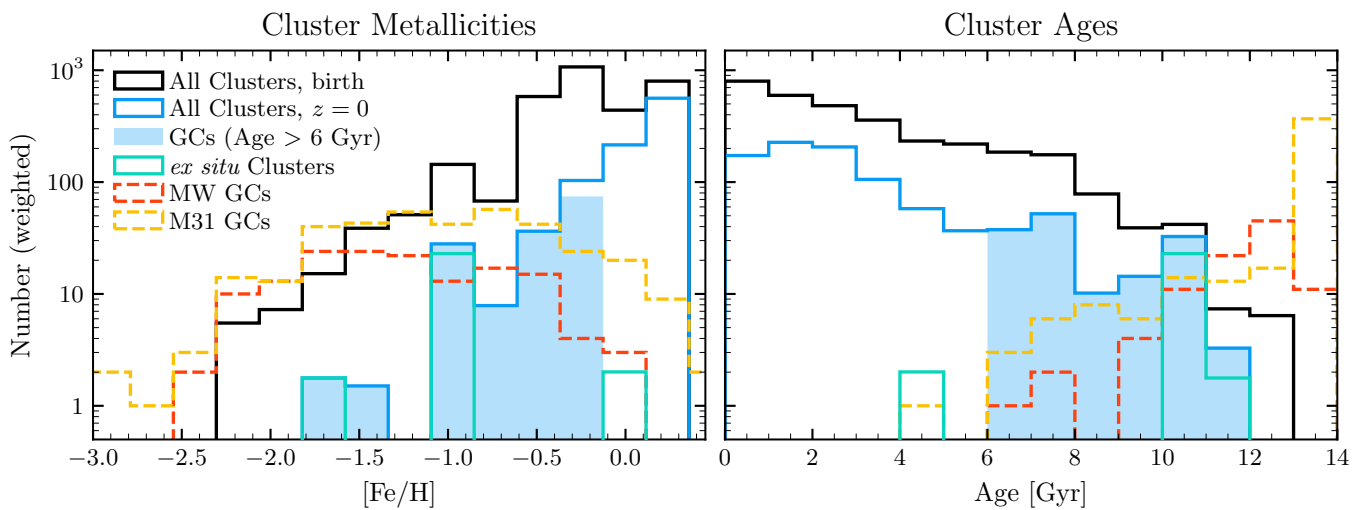


Figure 7. The distribution of metallicities and ages for our initial and final population of clusters. On the **left**, we show the cluster metallicities. Unlike both the MW and M31, our clusters are heavily weighted towards higher metallicities (though our GCs are still lower metallicity than the cluster population as a whole). This is especially true for *ex situ* clusters accreted from infalling dwarf galaxies (which we show in pale green). On the **right**, we show the distribution of cluster ages. As with our distribution of metallicities, the clusters in our catalog are significantly younger than the old GCs in both the MW and M31.

based estimates ($0.7 - 6M_{\odot}/\text{yr}$, Behroozi et al. 2013). Given the on average constant cluster-formation efficiency per stellar mass (Paper I, Figure 2), this can certainly explain the young and intermediate age cluster described in §4.1. At the same time, the large burst of massive cluster formation at $z \approx 0.8$ is largely driven by a late galaxy merger at that redshift, in contrast to the assumed merger history of the MW (where the last major merger was assumed to occur at $z \gtrsim 1.5$, Belokurov et al. 2020) (though we caution that not most starbursts occurring during the galaxy history are not associated with a merger). In addition, it has been shown that MW-mass galaxies in Local Group environments form stars earlier, particularly at $z \gtrsim 2$ (Santistevan et al. 2020), than isolated MW-mass galaxies. Efforts to explore the formation of GCs in Local Group-like structures are currently underway.

Of course, one key defining feature of GCs in the MW is that they are largely found on extended orbits in the halo (as opposed to younger open clusters that are preferentially found in the disk Portegies Zwart et al. 2010). While our GCs are younger and higher metallicity than those in the MW, we do find a clear distinction between the disk-inhabiting young clusters and the more isotropically distributed GCs. In Fig. 8, we show the relationship between the z component of the clusters’ orbital angular momentum about the galaxy (where the z direction is defined as perpendicular to the galactic disk) and the age of the clusters. While young (and high metallicity) clusters are largely co-rotating with the disk, the older clusters, formed during minor mergers and the earlier phases of galaxy assembly, appear to be on largely isotropic orbits, similar to the observed “blue”, metal-poor GCs in the MW. While this galaxy may not be representative of the MW or M31 in terms of its star formation or assembly history, it is clear that the orbits of the surviving older/metal poor GCs in our model show a similar pattern (e.g., Zinn 1985).

This pattern arises from two sources: first, we have limited our definition of GCs to those lying within 100 kpc of the galactic center at $z = 0$. But this definition also includes many clusters that were formed in distant dwarf galaxies, only to later migrate inward as their hosts were accreted by the main m12i galaxy. In the FIRE-2

simulations, every star particle is assigned a galaxy ID based on whichever galaxy the particle was closest to at its formation time. We define any GC that has an initial galaxy ID different than the main galaxy and a galactocentric distance at $z = 0$ of < 100 kpc as an *ex situ* GC. With our weighting scheme, this corresponds to 27 clusters, 25 of which are old GCs, or about 17% of the GC population at $z = 0$. This is compatible with the low end of estimates for the fraction of accreted GCs in the MW (~ 18 -32% Forbes & Bridges 2010). Our *ex situ* clusters are older (~ 10 Gyr) and more metal poor ($[\text{Fe}/\text{H}] \sim -1$) than our other GCs, as is apparent in Fig. 7. This is in excellent agreement with the ages and metallicities of the accreted MW GCs; however, in our case these clusters are older than the typical m21i GC, while in the MW these clusters occupy the younger of the two populations identified in Fig. 1 of Forbes & Bridges (2010).

Second, Fig. 8 shows that the *ex situ* GCs are not the only ones on isotropic or even retrograde orbits about the galaxy. Even the GCs formed at low initial R_{GC} in the main galaxy are on isotropic orbits. This is because while the present day orbits of *ex situ* clusters are set by the orbits of their infalling hosts, the orbits of the *in situ* CMC-FIRE clusters are largely set by the morphology and dynamical state of the galaxy at the time that the clusters formed. Approximately 6 Gyr ago, the MHD m12i galaxy transitioned from a bursty, chaotic phase of star formation to a smooth phase where most star formation occurred in the newly-formed thick disk (Ma et al. 2017; Stern et al. 2021; Yu et al. 2021; Gurvich et al. 2022)⁶. Because we have defined our GCs as those clusters older than 6 Gyr, they are preferentially formed on isotropically distributed orbits (following the velocity distribution of the gas, Gurvich et al. 2022), while the younger clusters are preferentially formed within the disk (though we emphasize that our choice of 6 Gyr was actually based upon the youngest GCs in the MW, and for consistency with the literature,

⁶ Note that while these references analyzed to the non-MHD version of the m12i galaxy, the MHD version we employ here also undergoes a similar transition (at 5.7 Gyr lookback time, instead of the 6.15 Gyr identified in Yu et al. 2021). See Fig. 1 of Paper I.

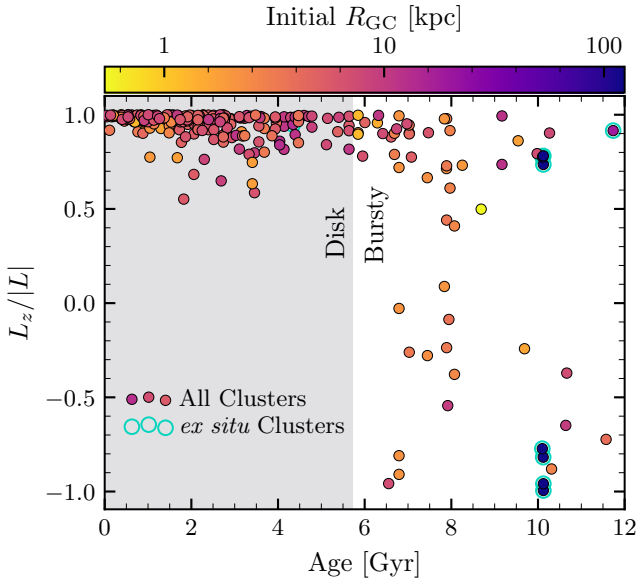


Figure 8. The relationship between the “co-rotation” of the surviving clusters’ orbits at $z = 0$ and their age. Here, we define co-rotation as the fraction of the cluster’s angular momentum about the galaxy that is aligned with the rotation of the galactic disk. Consistent with clusters in our own Galaxy, the youngest clusters preferentially rotate with the disk, while older clusters tend to be isotropically distributed. Finally, we indicate those clusters that were originally formed outside of the main galaxy with blue-green circles. These clusters are typically older, more metal poor, and isotropically distributed, consistent with their accretion history onto the main galaxy. We also show in shaded regions the transition from bursty star formation to disk star formation (which occurs as 6.15 Gyr lookback time in the non-MHD m12i galaxy studied in Yu et al. 2021, or approximately 5.7 Gyr in the MHD m12i galaxy studied here).

e.g., Pfeffer et al. 2018). Thus, we can conclude that the main differences between our GC population and that of the MW arise from the specific assembly history of the m12i galaxy itself. Had the transition occurred at an earlier time in m12i, our GC population would likely be closer in age and metallicity to those in the MW. This suggests that there may be a connection between the orbits of metal-rich and metal-poor clusters in the MW and the formation of the most massive GCs during the transition from bursty to disk star formation; we will explore this potential connection in a future work.

5 CLUSTER EVOLUTION AND DESTRUCTION

5.1 Galactic Morphology Controls Cluster Survival

Since cluster formation in this model traces the normal star formation of the m12i galaxy, it is hardly surprising that cluster orbits should be set by the morphology and dynamical state of the galaxy when they were formed. But even after the clusters are formed, the galaxy morphology has a significant effect on the long-term survival of GCs: clusters on elliptical or inclined orbits can experience significant tidal mass loss during close encounters with GMCs (e.g., Terlevich 1987; Gieles et al. 2006; Linden et al. 2021), transits through the galactic disk (e.g., Ostriker et al. 1972), encounters with galactic spiral arms (e.g., Gieles et al. 2007), and close pericenter passages about the galactic bulge (e.g., Spitzer 1987). Overall, we

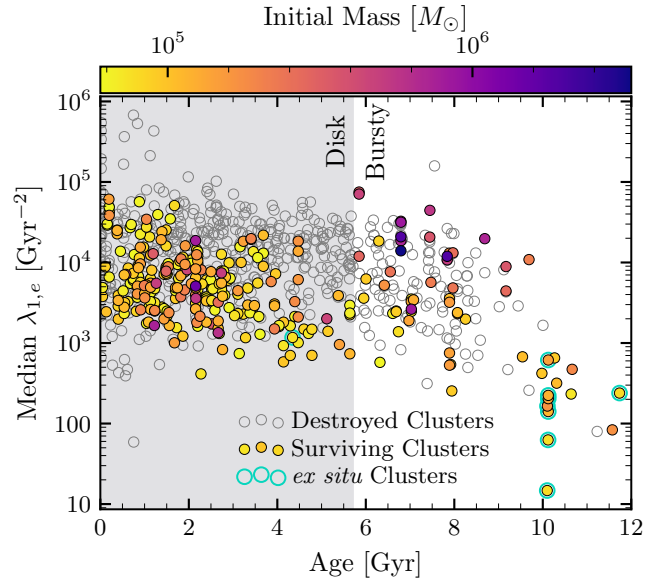


Figure 9. The relationship between the formation time of all clusters in our catalog to the median effective tidal field they experience over their lifetime (see §2.4). The open circles indicate clusters destroyed before $z = 0$, while the filled colors indicate those that survive to the present day. The color bar indicates the mass of the cluster at formation, with clusters formed *ex situ* outlined in blue-green.

expect clusters in the disk to experience stronger tidal fields, ensuring that they dissolve faster than their halo counterparts. Given our 6 Gyr dividing line between GCs and young clusters, this largely implies that our GCs should live, on average, longer than the massive young and open clusters formed once the galaxy transitions to a disk morphology.

In Fig. 9, we show the median tidal strength experienced by all of our clusters throughout their lifetime as a function of cluster age. The median tidal strength experienced by clusters is lowest during the earliest phases of galaxy formation, but as the galactic disk begins to assemble, the tidal strength steadily increases as m12i transitions from its bursty mode of star formation into a thick disk galaxy. Once clusters begin forming in the disk, the tidal field is largely constant, with a wide scatter determined by the cluster’s initial orbital position and eccentricity in the disk. This carves out a roughly triangular region in Fig. 9 where older clusters are more preferentially destroyed at higher median $\lambda_{1,e}$. This has important implications for the long-term survival (or lack thereof) of disk clusters, particularly the open clusters observed in the MW. A better understanding of this process will require both a higher-resolution tracking of the potential experienced by clusters in the disk and a real-time treatment of tidal shocking during the cluster integrations; see §2.4 and Appendix B.

The fact that clusters formed earlier in the process of galaxy assembly are more likely to survive creates an obvious mechanism for promoting GC survival over younger massive star clusters. Furthermore, clusters that were formed *ex situ* are also more likely to survive for longer periods, owing to their significantly wider halo orbits than clusters formed *in situ* (Fig. 10). Ironically, these clusters actually experience stronger tidal fields while still living in their birth galaxies; it is only after they are accreted by the main m12i galaxy that they experience sufficiently weak tidal fields to survive to the present day. This suggests that some *ex situ* clusters have *only*

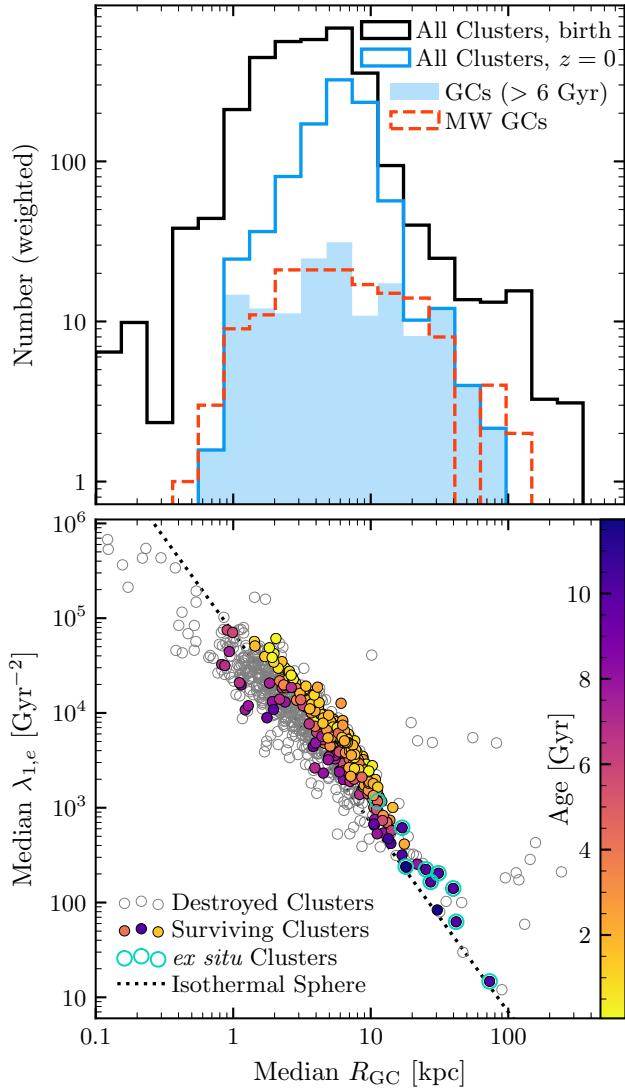


Figure 10. The galactocentric radii of the CMC-FIRE clusters and the tidal fields they experience. On the **top**, we show the distribution of median galactocentric distances for all clusters over their lifetimes (in black), as well as those that survive to $z = 0$ (blue line) and those surviving clusters we define as GCs (solid blue). We also show the galactocentric distances of the MW GCs from the [Harris \(1996, 2010\)](#) catalog. While these are not the same quantity, the median R_{GC} of an orbit over time represents a fair draw from the distributions of that orbit, making it a reasonable comparison to the MW GCs. On the **bottom**, we show the relationship between the median radii to the median effective tidal field they experience over their lifetime (see §2.4). The open circles indicate clusters destroyed before $z = 0$, while the filled colors indicate those that survive to the present day. The color bar indicates the age of the surviving clusters. We also show in dotted black the relationship between tidal strength and radius for clusters in an isothermal sphere with the same effective velocity dispersion as the m12i galaxy.

survived because of their accretion into a larger galaxy. This characteristic decrease in tidal field strength is shown in the example *ex situ* cluster in Fig. 1, and has been observed in previous studies of cluster formation in galaxy simulations ([Li & Gnedin 2019](#); [Meng & Gnedin 2022](#), and §5.3). This result suggests that accreted clusters in the MW and other galaxies may actually be a better tracer of old star formation in dwarf galaxies than clusters in present-day dwarf galaxies!

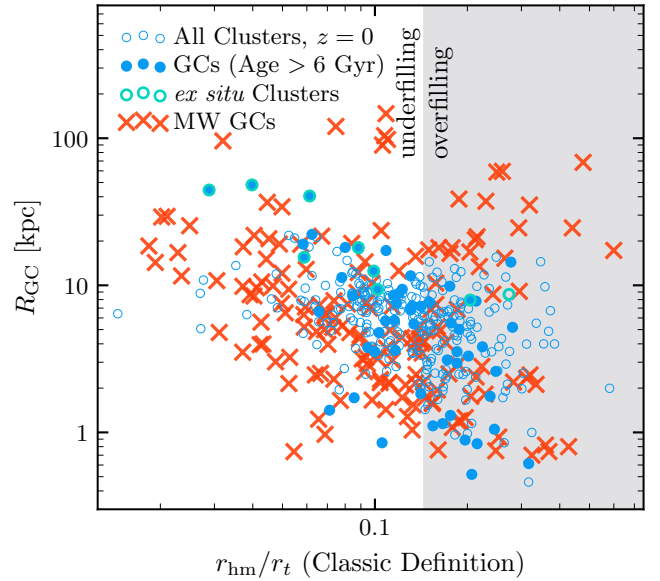


Figure 11. The relation between clusters that are tidally overfilling and their galactocentric distance, for both our model clusters (in open blue circles all clusters and filled blue circles for old GCs) and the MW GCs (red crosses). We also outline clusters formed *ex situ* in blue-green. The shaded region indicates clusters that are tidally overfilling (see discussion c.f. Fig. 2). Our GCs largely span the space of clusters in the MW, though we do not reproduce the tidally filling population at large galactocentric radii that [Baumgardt et al. \(2010\)](#) suggested are in the process of disrupting.

We note in Fig. 10 the excellent agreement between the median radial distribution of our CMC-FIRE clusters and the present-day radial distribution of GCs in the MW, and the strong correlation between the median $\lambda_{1,e}$ of the clusters and their median galactocentric distance. This correlation follows a roughly $1/R_{GC}$ power law, similar to the predicted tidal field experienced by clusters on circular orbits in an isothermal sphere, where $\lambda_{1,e} = 2\sigma^2/R_{GC}^2$ (and $\sigma \approx 180\text{km/s}$ is the effective velocity dispersion of the potential for the m12i galaxy). Taken together, this suggests that the tidal fields experienced by our CMC-FIRE population are representative of those experienced by the MW GCs.

Finally, it has been suggested ([Baumgardt et al. 2010](#)) that there exist two distinct populations of clusters beyond 8 kpc when viewed in the plane of galactocentric distance versus tidal filling: a compact population with r_{hm}/r_t less than 0.05, and a second population of tidally filling clusters with $0.1 < r_{hm}/r_t < 0.3$. We show this in Fig. 11. While we are able to reproduce the lower population in galactocentric radius, we do not seem to reproduce the population of tidally-filling, large distant clusters. ([Baumgardt et al. 2010](#)) suggested that these clusters in the MW were in the process of being disrupted. Given that the closest clusters from our population are all *ex situ* clusters, this population may also simply be the remnants of a dwarf galaxy accreted by the MW (for which m12i has no counterpart).

5.2 Cluster Structure as Determined by Black Holes

Over the past decade, a growing consensus has been developing that the overall size of a GC's core, and the ratio between the core and half-mass (or half-light) radii, is determined by the number of the black holes (BHs) that have been retained by the cluster up to the

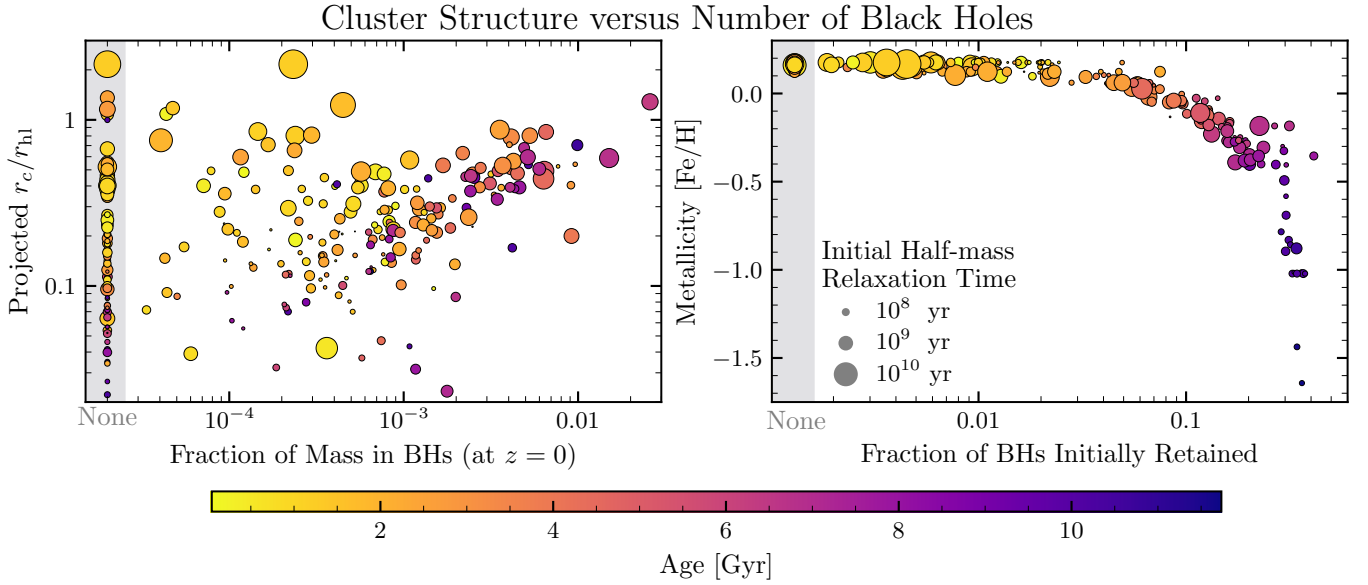


Figure 12. The structural parameters of the clusters that survive to the present day and their dependence on the fraction of black holes that are initially retained. We define the BH retention fraction as the number of black holes that remain bound to the cluster immediately after the collapse/supernova of their progenitor stars, divided by the total number of black holes formed. Note that we exclude BHs formed through mergers involving other BHs. The size of each point indicates the cluster’s initial half-mass relaxation time (Equation 8), while the color indicates the age of the cluster in Gyr. On the **left** panel, we show the relationship between r_c/r_{hl} and the fraction of BHs that have been retained up to the present day. Older clusters follow a roughly linear correlation, with clusters with significant mass in BHs have larger core radii compared to those with fewer BHs. However, most younger clusters have a mass fraction in BHs $\lesssim 10^{-3}$ and larger core radii. On the **right**, we show why this is the case: clusters that are younger have higher metallicities and retain fewer of their BHs at birth because of the larger supernova natal kicks associated with less-massive BHs.

present day. A cluster only reaches “core collapse” (defined observationally as having a SBP that increases continuously towards the cluster center) once it has ejected nearly all of its initial BHs (Merritt et al. 2004; Mackey et al. 2008; Breen & Heggie 2013; Kremer et al. 2018). Both analytic arguments (Breen & Heggie 2011) and numerical simulations (Breen & Heggie 2013; Arca Sedda et al. 2018; Kremer et al. 2019) have shown that the ejection rate of BHs is largely controlled by the relaxation time of the cluster at the half-mass radius, given by (e.g., Spitzer 1987):

$$T_{\text{rlx}} = 0.138 \frac{N}{\log \Lambda} \left(\frac{r_{\text{hm}}^3}{GM} \right)^{1/2}, \quad (8)$$

at the cluster’s half-mass radius⁷. Because clusters require BH “burning” to supply the energy to hold the cluster against continued gravothermal collapse (producing the flat core profiles characteristic of the King or Plummer models), the clusters with the largest cores are expected to be those with longer relaxation timescales, that have been unable to eject all of their BHs by the present day. In other words, GCs with smaller cores are thought to be dynamically older, having had many relaxation times over which to eject their BH subsystems.

But then how are we to understand distribution of r_c/r_{hl} and concentration parameters presented in Fig. 6, where our GCs are more compact than those in the MW, despite being younger overall? In Fig. 12, we show the relationship between fraction of mass in BHs for our $z = 0$ cluster population and the ratio of the core to half-mass

radii. For the dynamically old clusters, the relationship is nearly linear, in good agreement with previous results that have studied the presence of BH subsystems in GCs and their observational properties (Morscher et al. 2015; Kremer et al. 2019; Weatherford et al. 2020). However, we note that there also exists a population of younger clusters that do not appear to lie on this linear trend.

This feature actually arises from a complex interplay between the age-metallicity relationship of the m12i galaxy and the initial retention of stellar-mass BHs. Younger clusters have higher stellar metallicities, which in turn drive stronger winds for the massive stars in the clusters at birth. However, this means that the BHs that are formed from collapsing stars are typically lower mass ($\lesssim 15M_{\odot}$) than those formed in low-metallicity clusters (which are thought to produce many of the “heavy” 30-40 M_{\odot} BHs observed by LIGO/Virgo). The supernova that form these lower-mass BHs produce large amounts of ejecta (according to the standard prescriptions available in COSMIC, from Fryer et al. 2012), which in turn impart larger natal kicks to the BHs at birth (as high as the ~ 400 km/s kicks experienced by neutron stars, Hobbs et al. 2005). This is in contrast to the 30 M_{\odot} BHs formed in low-metallicity environments, which are largely thought to form via direct collapse (Fryer & Kalogera 2001). As a result, higher-metallicity GCs and young clusters retain fewer BHs after ~ 20 Myr, and can dynamically eject their remaining BH population faster.

This relationship is shown explicitly in the right panel of Fig. 12. Clusters with metallicities above solar (roughly those 4 Gyr or younger) retain at most 10% of their BHs initially. This correlation has a far stronger influence on the initial retention of BHs than either the cluster mass or initial radius (which directly effect both the initial half-mass relaxation time and the cluster escape speed). Only a handful of clusters are so massive that they deviate from the trend

⁷ Note that $\log \Lambda$ here is the Coulomb logarithm for the internal cluster evolution, typically assumed to be $\log(\gamma N)$ with $\gamma = 0.01$.

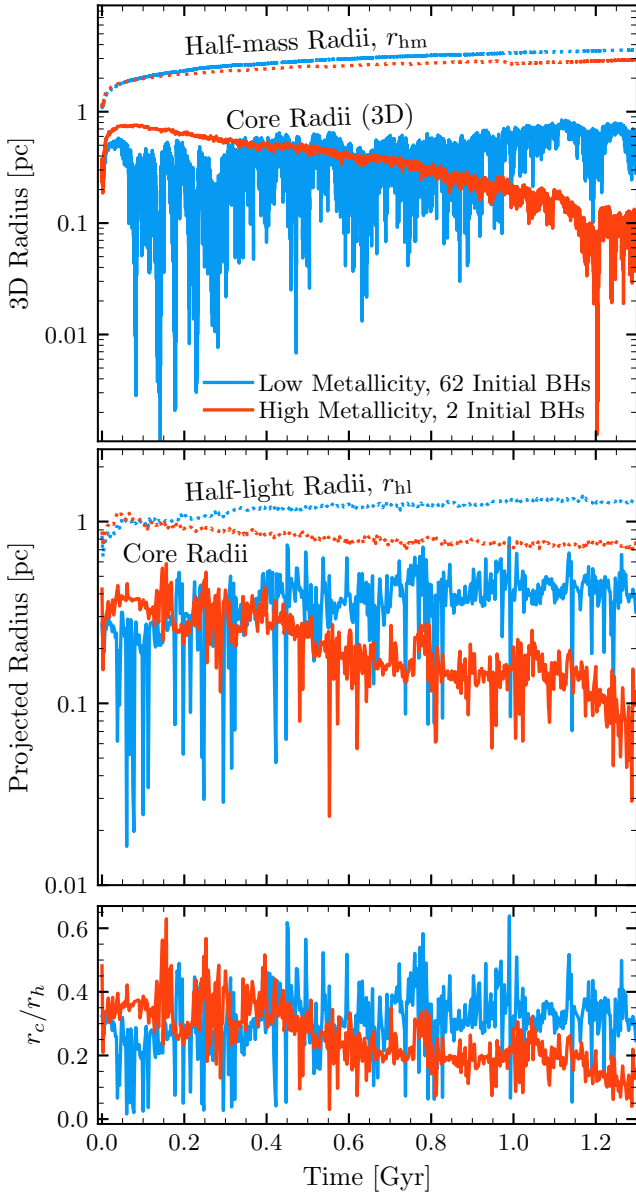


Figure 13. The core and half-mass/light radii for two typical clusters ($N \approx 10^5$, virial radius ≈ 2 pc, $\gamma \approx 3$), whose primary difference is their birth redshifts ($z = 0.9$ for blue and $z = 0.1$ for red) and the number of BHs they initially retain. On the **top**, we show the theoretical 3D core and half-mass radii, while in the **middle** we show the projected 2D core and half-light radii. Here, the model with 62 BHs collapses quickly, but then rapidly re-expands due to heating from BH burning. The model with 2 BHs, on the other hand, collapses much more slowly, but does not re-expand. As a result, the cluster appears core collapsed at a much younger age than its metal-poor counterpart, which does not appear core collapsed until it is ~ 4.5 Gyr old (not shown). Finally, on the **bottom**, we show the ratio of the core- to half-light radii.

(e.g. the *Behemoth* cluster previously described in Rodríguez et al. 2020). It is immediately clear that the younger clusters will never follow the linear relationship between M_{BH} and r_c/r_{hl} , because they do not have a significant number of BHs to begin with! Our GCs—with a median age of ~ 8 Gyr—are able to retain more (10% - 20%) of their initial BHs. But this is still a factor of ~ 2 below the

BH retention for the truly old, metal poor GCs (like those observed in the MW).

What this means is that, despite being younger, our GCs appear dynamically older and more core collapsed than those in the MW. Indeed, for clusters that begin with very few BHs, the picture of core collapse resembles the more classical picture of GC evolution (e.g., Spitzer 1987), where, for a Plummer sphere with equal masses, the core-collapse time is approximately $16t_{\text{rlx}}$ (e.g., Freitag & Benz 2001, and references therein). To illustrate this, we pick two clusters, one old and one young, with nearly identical initial conditions— $\sim 10^5$ stars, 2 pc virial radii, and Elson γ parameters of ~ 3 —and plot the evolution of their radii over time in Fig. 13. Of course, because of their different cosmic birth times ($z = 0.9$ versus $z = 0.1$), the old cluster was born with a metallicity of $0.5Z_{\odot}$ and retains 62 BHs initially, while the young cluster was born with a metallicity of $2Z_{\odot}$ (which we truncate to $1.5Z_{\odot}$, see §2.3) and retains only 2 BHs. In the old cluster, the *initial* core collapse occurs within ~ 75 Myr. This first collapse is driven by the mass segregation of the BHs, which scales as

$$T_{\text{cc}} \approx \frac{\langle m \rangle}{m_{\text{BH}}} T_{\text{rlx}} \quad (9)$$

where m_{BH} is the mass of the BHs (or the most massive objects in the cluster) and $\langle m \rangle$ is the average stellar mass. However, immediately after core collapse, the core suddenly re-expands as the energy generated by the formation of BH binaries is injected into the cluster core. While the initial collapse is visible in the 3D core radius, it is barely detectable (beyond standard fluctuations) in the observed core radius shown in the bottom panel of Fig. 13. This cluster will not undergo a true, permanent core collapse (sometimes called “second core collapse”, Breen & Heggie 2013; Heggie 2014) until much later (4.5 Gyr after its formation, not shown here).

On the other hand, the younger cluster, being deprived of any BH subsystem by natal kicks, only experiences a single core collapse event. In Fig. 13, this occurs at approximately 1.2 Gyr (or $6 T_{\text{rlx}}$, where $T_{\text{rlx}} = 200$ Myr for this cluster) after formation. This is closer to the $16 T_{\text{rlx}}$ core collapse time for equal-mass clusters (with the remaining difference arising from the non-equal mass stellar IMF, e.g., Spitzer & Hart 1971; Inagaki & Saslaw 1985; Gieles et al. 2010), but still significantly faster than the 4.5 Gyr collapse time for the older low-metallicity cluster. Despite its age, the younger cluster appears dynamically older than its older sibling. This counter-intuitive result suggests that one must be cautious when using GCs as tracers of galactic star formation and evolution, since any measurement of their dynamical age strongly depends upon the initial retention of BHs and the age-metallicity relation of their birth galaxies in addition to their initial relaxation time as determined by their birth masses and radii.

Finally, it should be noted that our analysis has utilized almost exclusively a relatively new understanding of GC evolution, where a GC’s core radius is largely determined by the size of its BH subsystem (e.g., Mackey et al. 2008; Breen & Heggie 2013; Heggie 2014; Kremer et al. 2019), which disperses over a timescale set by the cluster’s half-mass relaxation time, c.f. Equation (8). Of course, this new framework relies on the initial presence of a large BH population; in the absence of these BHs (as occurs in our high-metallicity clusters), the size of a cluster’s core is instead determined by the classic “binary burning” of primordial stellar binaries in the central regions of the core (e.g., Gao et al. 1991; Wilkinson et al. 2003; Chatterjee et al. 2010), which in turn would suggest a dependence on the initial binary fraction of our simulations (10%, see

§2.2). However, recent observational evidence (Moe et al. 2019) has shown that binary fraction (for close solar-type stars) is largely anti-correlated with metallicity, decreasing to $f_b \lesssim 25\%$ above $[\text{Fe}/\text{H}]$ of -0.5 (where our cluster models in Figure 12 retain less than 10% of their initial BHs) cluster. Secondly, detailed N -body simulations (Heggie et al. 2006, Fig. 17 and 18), have shown that the primordial binary fraction does not significantly change either r_c/r_{hm} or the core collapse time (unless the primordial binary fraction is zero), at least not before the clusters can be tidally disrupted (Trenti et al. 2007). As such, we conclude that our primordial binary fraction does not significantly influence the results presented here.

5.3 Comparison of GC Survival to Other Studies

Many previous studies have explored the long-term evolution and survival of the MW GC system, both using observations of our own Galaxy (using the best-available knowledge of its galactic potential, e.g., Gnedin & Ostriker 1997; Long et al. 1992; Chernoff & Weinberg 1990; Prieto & Gnedin 2008; Vesperini & Heggie 1997; Baumgardt 1998), and cosmological simulations of MW-like galaxies (e.g. Rieder et al. 2013; Pfeffer et al. 2018; Li et al. 2017). The initial results here occupy a unique space in this pre-existing literature: on the one hand, our models of star cluster evolution are the highest resolution of any presented so far, including realistic prescriptions for stellar evolution, binary formation and interactions, and realistic surface brightness profiles to compare directly to observations. Of course, this precision comes at a cost, as we have only simulated a single galaxy’s cluster system. As such, it is important to compare our results to other cosmological studies of cluster formation in MW-mass galaxies, as well as studies of the MW GC system itself.

The first obvious comparison is between our results and those of the E-MOSAICS simulations (Pfeffer et al. 2018). In this series of simulations, the authors explored the populations of GCs formed in several MW-mass galaxies in the EAGLE simulations. Starting from those initial star clusters, they then follow the evolution and destruction of clusters from birth to $z = 0$ using semi-analytic prescriptions for the cluster’s mass and radius and its subsequent evolution in a time-varying galactic potential (based on the models of Kruijssen et al. 2011). While N -body cluster evolution models are more sophisticated in their internal physics, our method of computing the tidal fields experienced by the clusters and their dynamical friction timescales are both taken directly from Pfeffer et al. (2018). See §2.4 and Appendix B, though note that our modeling of tidal shocking is done in post-processing, and does not follow the instantaneous increase in cluster radius.

In the left panel of Fig. 14, we compare our initial and final CMFs to those from the 10 MW-like cluster systems of the E-MOSAICS simulations. Both the initial masses of our full catalog and the reduced ICMF of the 895 clusters we evolved here are consistent with the masses of clusters identified by E-MOSAICS (see Paper I for a more in-depth discussion). When comparing our $z = 0$ mass function, we find consistency between our results, despite the different choices we employed in calculating the dynamical friction timescales (see the discussion in §2.4) and our limited treatment of tidal shocking. Like the present study, the GCMFs presented in Pfeffer et al. (2018) only considers clusters older than 6 Gyr to be true GCs. When comparing only GCs, we find a decrease in lower-mass clusters compared to E-MOSAICS, particularly around the peak ($\sim 4 \times 10^5 M_\odot$) of our GCMF.

On the one hand, our GCMF is arguably closer in number to the number of GCs in the MW (148 vs 157) than the E-MOSAICS simu-

lations. However, this could easily be a byproduct of our $6 \times 10^4 M_\odot$ cutoff in our simulated initial CMF (i.e. had our ICMF extended down to $10^4 M_\odot$, we may have produced more low-mass GCs). But at the same time, the number density of CMC-FIRE clusters at $\sim 10^5 M_\odot$ is closer to that of the MW than the E-MOSAICS GCMFs (while the number density of M31 GCs at that mass lies roughly between both models). While it is difficult to disentangle the effects of galaxy-to-galaxy variation here, it is obvious that we produce fewer GCs across all masses than the E-MOSAICS simulations. However, we note that both the E-MOSAICS GCMFs and our CMC-FIRE GCMF peak significantly below the GCMFs of the MW or M31, indicating that both approaches either form too many low mass clusters or are insufficiently efficient at destroying them.

This is also suggested by comparisons to the ART simulations (Li et al. 2017, 2018; Li & Gnedin 2019), which use high-resolution hydro simulations of MW-mass galaxies to study the formation and evolution of star clusters formed before $z = 1.5$. In the right panel of Fig. 14, we show the $z = 0$ GCMFs from Fig. 4 of Li & Gnedin (2019) and compare it to our own CMF and GCMF. Here, the different GCMFs represent star cluster systems from simulations with different star-formation efficiencies, while the solid and dashed bands represent different assumptions for the strength of the galactic tidal field (see Li & Gnedin 2019, for details). Limiting ourselves only to old GCs, we find that our GCMF is equivalent to one found in either a galaxy with high star-formation efficiency and strong tides (i.e. a high destruction rate) or low star-formation efficiency and weak tides, both of which produce a decrease in the number of GCs surviving to the present day. We note that the galaxies do not show a late transition from bursty to disk-based star formation like the m12i galaxy, possibly because the galaxy simulations themselves did not proceed beyond $z = 1.5$. But at the same time, we do find the same trend for the tidal fields experienced by individual clusters to decrease over time (particularly for those clusters accreted from infalling dwarf galaxies; see §5.1 and Fig. 1). This is consistent with the mechanism proposed in Kruijssen (2014); Forbes et al. (2018), where GCs rapidly migrate from gas-rich environments (where they are formed) following galaxy mergers to regions with lower tidal field strength, thereby promoting their long-term survival.

However, we do not find the same trend of decreasing tidal field for the *in situ* clusters identified by Meng & Gnedin (2022). While this may be because of our treatment of the tidal field in the initial m12i snapshot (see footnote in §2.4), the present study’s measurement of the tidal tensors (with typical separations of ~ 6.5 pc) is significantly higher resolution than the $O(100)$ pc resolution of either the E-MOSAICS or ART simulations, and would allow us to resolve the early tidal effects of star-forming regions. More likely, we believe this is because our *in situ* clusters do not show the same trend of outward migration identified in their study. Since both studies (as well as E-MOSAICS) use tracer particles from the cosmological simulation to extract the tidal fields, these differences likely arise from the different evolution of the cosmological simulations themselves. It should also be noted that the ART simulations use a different approximation for the tidal field experienced by the clusters (using the maximum absolute value of the Eigenvalues of the tidal tensor, instead of the $\lambda_{1,e}$ that we and E-MOSAICS use), which can be a factor of ~ 2 lower than our approach (See Meng & Gnedin 2022, Appendix B). While our approximation has been shown to accurately reproduce the tidal fields from a spherical Plummer potential (See Figure C1 from Pfeffer et al. 2018), we note that both approaches are necessary simplifications from the true tidal field. Future work (di Carlo et al., in prep.) will explore the validity

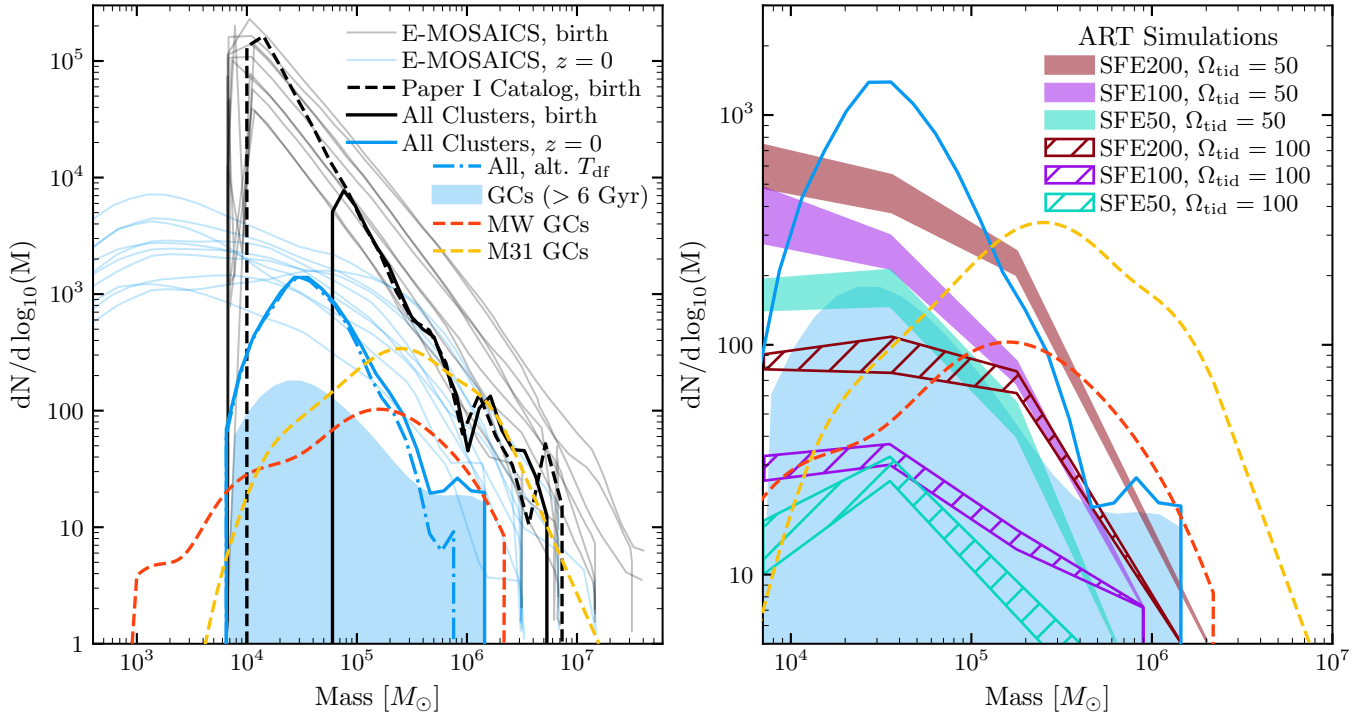


Figure 14. Comparisons between the mass functions of our CMC-FIRE clusters and the E-MOSAICS and ART simulations. On the **left**, we show the ICMF and GCMF from 10 MW-mass galaxy cluster systems in the E-MOSAICS models (Fig. 16 from Pfeffer et al. 2018). We show two ICMFs: the full ICMF from Paper I (dashed black), and the reduced ICMF of 895 clusters that were employed here (solid black, and multiplied by the weights described in §2.3). Note that the GCMF from E-MOSAICS only includes clusters older than 6 Gyr. To better compare, we show our full population of surviving clusters in solid blue, and our population of surviving clusters older than 6 Gyr in dotted blue. We also show the mass functions from the MW (Harris 1996, 2010 edition) and from M31 (Caldwell et al. 2011). On the **right**, we show the results of comparisons between our models and the GCMF distributions from the ART simulations (Li & Gnedin 2019, Fig. 4), including the mass functions for several different galaxy formation simulations and assumed tidal strengths.

of these prescriptions when compared to N -body integrations in a realistic galactic tidal potential.

While previous studies have suggested that tidal fields, and particular tidal shocking, play a critical role in sculpting the $z = 0$ GC populations, our results are substantially less definitive. As stated in §2.4 and Appendix B, our post-processing analysis suggests that only one of our 895 clusters would have been destroyed from the injection of energy by tidal shocking, and even then, that cluster was destroyed by our tidal stripping prescription at the same time that our shocking analysis predicted its destruction. Of course, it is unsurprising that these two effects are linked: both are computed directly from the tidal tensor (Equation 4), and any significant change in the tidal tensor that would inject energy into the cluster would *also* be accompanied by a reduction in the tidal boundary, instantaneously removing a significant fraction of the cluster mass from our simulations.

In previous studies, the cumulative effects of evaporation, tidal shocking, and dynamical friction on the survival of the MW GC system have been explored by the use of “vital diagrams”, where the typical destruction rate of clusters is given by the sum of the destruction rate for the three processes. Assuming that the rate of cluster destruction by each mechanism can be expressed as the inverse of the typical timescale for destruction by that mechanism, the vital diagram for clusters can be computed as the level sets of the function

$$\frac{1}{T_{\text{dest}}} = \frac{1}{T_{\text{rlx}}} + \frac{1}{T_{\text{ts}}} + \frac{1}{T_{\text{df}}} \quad (10)$$

where, to study the old clusters in our own Galaxy, T_{dest} is typically set to a Hubble time (or 10 Gyr in Gnedin & Ostriker 1997).

In Gnedin & Ostriker (1997), these diagrams were generated using fits to the orbits and masses of MW GCs, along with a model for the MW gravitational potential. The level sets of Equation (10) were then computed for different initial galactocentric radii (adjusting both the tidal field strength in the given potential and the rate and strength of tidal shocking). In Fig. 15, we show the vital diagrams from Gnedin & Ostriker (1997) in (3D) mass and radius space and compare them to our own CMC-FIRE population. The initial population spans several orders of magnitude in radius when compared to the predictions, but our final population agrees reasonably well with the vital diagrams for the MW. In particular, if we restrict ourselves to old GCs (close to the ~ 10 Gyr lifetime considered in the original study), our results agree extremely well with the original predictions of Gnedin & Ostriker (1997), arguably better than the actual MW!

However, this result is somewhat shocking, as we have not included any run-time prescription for tidal shocking in the models. Instead, our models replace both the evaporation and tidal shocking timescales with the time-varying change in the tidal boundary of the cluster. This process appears to work surprisingly well, destroying many of the clusters that were born in the region where tidal shocking should have operated. However, because of the difference in ages between our GC population and the MW, as well as the approximations made in our implementation of the external tidal potential within CMC, it is not immediately obvious if this truly

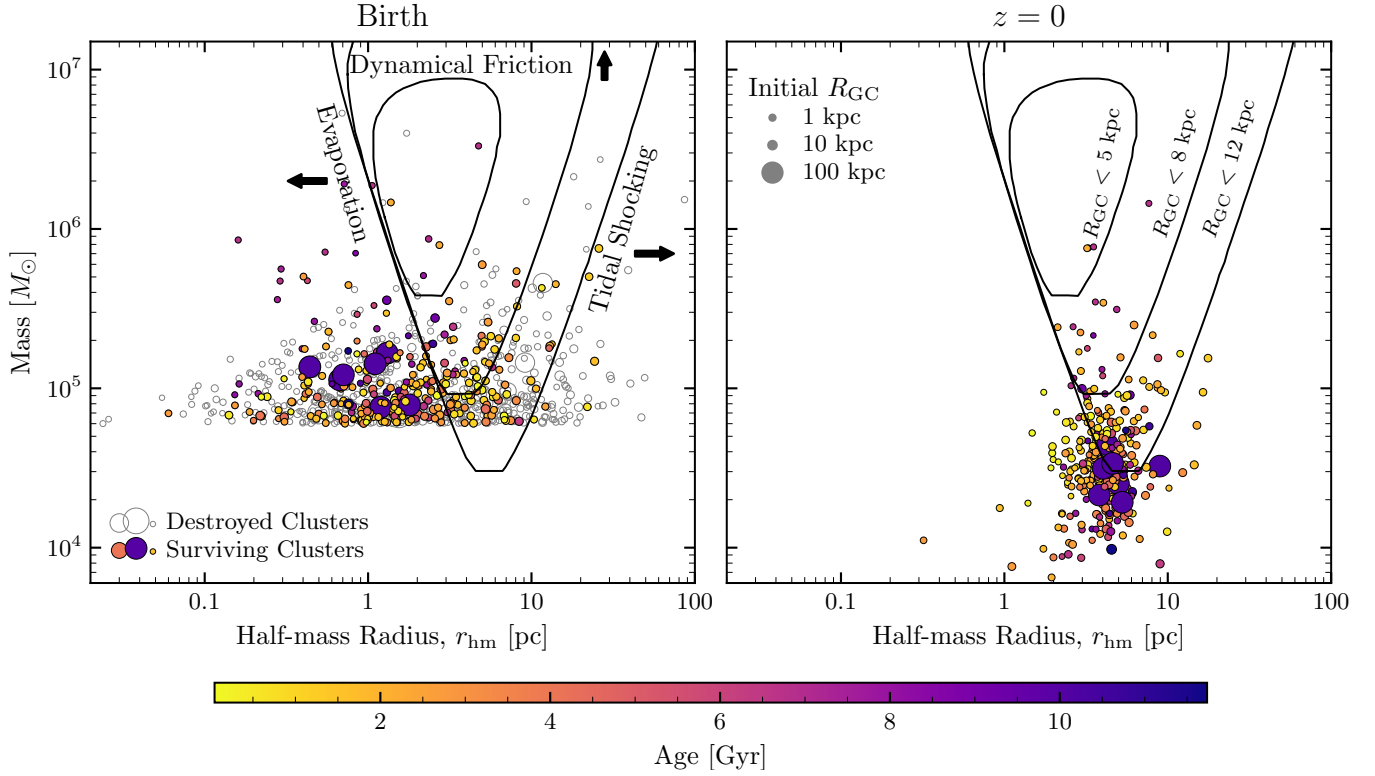


Figure 15. The distribution of our cluster populations in mass-radius space (note we use the real 3D half-mass radius of each cluster). On the **left**, we show the initial distribution of clusters (with disrupted clusters shown with gray circles), while the **right** shows the population that survives to $z = 0$. The filled color of the surviving clusters indicates their age, while the size indicates the initial galactocentric radius at which each cluster was formed. Finally, the black lines show the original vital diagrams from [Gnedin & Ostriker \(1997\)](#) based on the galactic model of [Ostriker & Caldwell \(1983\)](#), assuming isotropic velocities. Each of the three sides of the triangles show the region beyond which the process indicated with arrows would cause a cluster to be destroyed within 10 Gyr (e.g. clusters that lie to the right of the triangles will succumb to tidal shocking within a Hubble time, and so on).

means that tidal shocking does not operate on the GC population, or if our initial conditions largely occupy a region of $M - r_{\text{hm}}$ space that is unaffected by tidal shocking. By the same token, however, it is also possible that the MW clusters themselves were born in a region largely impervious to tidal shocking, and that while the process may be important in some regions, it is largely absent in the formation of our own Galaxy. Work exploring the effects of tidal shocking using direct N -body simulations is currently underway.

Lastly, we can use these comparisons as an opportunity to explore the implications of our prescription for dynamical friction. As previously stated (§2.4), while our computation of T_{df} is identical to that employed in [Pfeffer et al. \(2018\)](#), our criterion for termination is less strict, since we require the cluster to have an age older than the time-integrated value of T_{df} before it is considered destroyed (whereas the E-MOSAICS simulation assumes any cluster where the instantaneous values of T_{df} is greater than the cluster age is destroyed). In Fig. 14, we show the effect that adopting the E-MOSAICS prescription would have on our CMF⁸. This increases the number of clusters that are destroyed by dynamical friction from 4 to 45, though we note that in neither case is dynamical friction the dominant destruction mechanism for star clusters. In reality, of course, neither prescription is accurately capturing the change in the

cluster’s orbit due to dynamical friction. These choices will have important implications for the survival of the most massive clusters, as well as the creation of nuclear star clusters found in the centers of many galaxies (many of which are thought to have formed from the infall of massive GCs, eg., [Tremaine et al. 1975](#); [Neumayer et al. 2020](#)).

6 CONCLUSION

We have presented the first end-to-end simulation of massive star clusters that combines realistic star-by-star N -body simulations with a GMC-resolving cosmological simulation of galaxy evolution to model cluster evolution and destruction. Starting from the MHD m12i Latte simulation from the FIRE-2 suite of galaxy models, in [Paper I](#) we identified all of the collapsing GMCs and, using a catalog of high-resolution cloud-collapse simulations as a guide, developed an initial population of 73,461 YMCs formed throughout the galaxy across cosmic time. In this paper, we evolved 895 of the most massive clusters ($\sim 30\%$ of those more massive than $6 \times 10^4 M_{\odot}$) to the present day using the masses, radii, concentrations, metallicities, and birth times as initial conditions for our CMC integrations. To account for the continued influence of the galaxy on the star clusters, we included prescriptions for time-dependent tidal mass loss into our N -body code, where the tidal fields were calculated from the gravitational potential experienced along the orbit of a test particle that comprised the parent GMC.

⁸ Though note that our implementation is actually *more* strict than the E-MOSAICS assumptions, since here we calculate T_{df} assuming the initial mass of the cluster is fixed

Our cluster model predicts a total of 941 clusters in the galaxy by the present day, 148 of which we define as classical GCs (older than 6 Gyr). These GCs were all formed during the early phases of galaxy assembly, where star formation occurred in a bursty fashion, or in dwarf galaxies which were later accreted by the host galaxy. As a result, these clusters are largely on orbits that are isotropically distributed about the galactic disk. The younger clusters, meanwhile, are largely formed once the galaxy transitions to a disk profile and largely lie within the disk (where they experience tidal fields that are, on average, stronger than those on isotropic halo orbits).

Our $z = 0$ GC population still shows several key differences from GCs observed in the MW or M31. The CMC-FIRE GCs that formed *in situ* in the main galaxy are younger on average (with a median age of 7.9 Gyr) than those in the MW or M31, while the clusters created, *ex situ* (those accreted from dwarf galaxies) are largely consistent in number and with similar ages and metallicities to those in the MW. The most massive clusters in our catalog are formed *in situ* at $z \sim 0.8$ during a minor merger between a dwarf galaxy and the main m12i disk galaxy. Because of their age, the bulk of our GCs tend to be less massive than those in the MW, since clusters formed later in the process of galaxy assembly experience stronger tidal fields, on average, than those formed during early bursty phases of star formation (or GCs accreted from infalling dwarf galaxies). Furthermore, the later formation times of our GCs means they also form with higher stellar metallicities ($[\text{Fe}/\text{H}] \sim -0.4$) than many GCs in the MW. These higher metallicities lead massive stars in our clusters to lose more mass to stellar winds, producing BHs with lower masses than those expected to form in low-metallicity GCs. This, in turn, leads to higher BH natal kicks, reducing the number of retained BHs and accelerating core collapse in these clusters (despite their younger ages).

While these differences mean our GC population is not a perfect comparison to the GCs in the MW, the CMC-FIRE clusters offer an illuminating link between the ages, masses, metallicities, and radii of GCs in galaxies and the star formation and assembly histories of those galaxies. Orbits of present-day *in situ* clusters are largely set by the mode of star formation the galaxy was in when the clusters were born. In the m12i galaxy, all our GCs were formed during the bursty phase of star formation and retain their isotropically-distributed halo orbits up to the present day. In other galaxies, such as the MW, the transition from bursty to disk-based star formation may have occurred while GCs were still forming, creating a correlation between the age/metallicity of GCs and their orbits. The age/metallicity relationship is also encoded in the radii of the surviving clusters: since higher-metallicity clusters retain fewer stellar-mass BHs at birth, and undergo core collapse more rapidly, suggesting that cluster radii, in addition to masses and numbers, are a key tracer of star formation and galaxy assembly at high redshifts. This, in particular, is uniquely possible because of our N -body approach to modeling GCs (with its detailed treatment of single and binary stellar evolution).

Several previous studies have explored the evolution and destruction of star clusters in cosmological simulations using semi-analytic treatments of the cluster evolution (e.g., Li et al. 2017; Pfeffer et al. 2018; Li et al. 2018; Li & Gnedin 2019). This study represents the first attempt to attack this problem from the realm of collisional N -body modeling of star clusters. In doing so, we can not only answer questions about the formation, evolution, and survival of the MW and other GC systems, but we can begin to perform systematic studies of the internal properties of GCs and their potential contribution to many transients observed in the local universe. In a followup study (Lamberts et al., in prep.), we will

explore the implications of these realistic initial conditions and our treatment of cluster evolution and destruction on the production of gravitational-wave sources.

ACKNOWLEDGMENTS

The authors are grateful to Mike Boylan-Kolchin, Jeremy Webb, Sterl Phinney, Kyle Kremer, Fred Rasio, and Katie Breivik useful discussions. CR was supported by NSF Grant AST-2009916 and a New Investigator Research Grant from the Charles E. Kaufman Foundation. ZH was supported by a Gary A. McCue postdoctoral fellowship at UC Irvine. MYG was supported by a CIERA Postdoctoral Fellowship and a NASA Hubble Fellowship (award HST-HF2-51479). AL acknowledges funding from the Observatoire de la Côte d’Azur and the Centre National de la Recherche Scientifique through the Programme National des Hautes Energies and the Programme National de Physique Stellaire as well as the ANR COSMERGE project, grant ANR-20-CE31-001 of the French Agence Nationale de la Recherche. CAFG was supported by NSF through grants AST-1715216, AST-2108230, and CAREER award AST-1652522; by NASA through grant 17-ATP17-0067; by STScI through grant HST-AR-16124.001-A; and by the Research Corporation for Science Advancement through a Cottrell Scholar Award. AW received support from: NSF via CAREER award AST-2045928 and grant AST-2107772; NASA ATP grant 80NSSC20K0513; HST grants AR-15809, GO-15902, GO-16273 from STScI. This work used the Extreme Science and Engineering Discovery Environment (XSEDE), which is supported by National Science Foundation grant number ACI-1548562. Specifically, it used both the Bridges-2 system, which is supported by NSF award number ACI-1928147 at the Pittsburgh Supercomputing Center (PSC), and the San Diego Supercomputing Center Comet cluster under XSEDE allocation PHY180017. Additional computations were run on the FASRC Cannon cluster supported by the FAS Division of Science Research Computing Group and by the Black Hole Initiative (funded by JTF and GBMF grants), both at Harvard University. This work also used computational resources provided by TACC Frontera allocations AST-20019 and AST-21002. Images of the m12i galaxy were generated with FIRE studio (github.com/agarovich/FIRE_studio), an open source Python visualization package designed with the FIRE simulations in mind.

DATA AVAILABILITY

The data supporting the plots within this article are available upon request to the corresponding author. A public version of the CMC code is available at <https://clustermontecarlo.github.io/>.

REFERENCES

- Aarseth S. J., 2003, *Gravitational N-Body Simulations*, by Sverre J. Aarseth, pp. 430. ISBN 0521432723. Cambridge, UK: Cambridge University Press, November 2003.
- Aarseth S. J., Hénon M., Wielen R., 1974, *A&A*, **37**, 183
- Ambartsumian V., 1937, *Astronomicheskii Zhurnal*, **14**, 207
- Arca Sedda M., Askar A., Giersz M., 2018, *MNRAS*, **479**, 4652
- Baumgardt H., 1998, *A&A*, **330**, 480
- Baumgardt H., 2001, *MNRAS*, **325**, 1323
- Baumgardt H., 2017, *MNRAS*, **464**, 2174
- Baumgardt H., Hilker M., 2018, *MNRAS*, **478**, 1520

- Baumgardt H., Hut P., Makino J., McMillan S., Portegies Zwart S., 2003, *ApJ*, **582**, L21
- Baumgardt H., De Marchi G., Kroupa P., 2008, *ApJ*, **685**, 247
- Baumgardt H., Parmentier G., Gieles M., Vesperini E., 2010, *MNRAS*, **401**, 1832
- Behroozi P. S., Wechsler R. H., Conroy C., 2013, *ApJ*, **770**, 57
- Belczynski K., Dominik M., Bulik T., O’Shaughnessy R., Fryer C., Holz D. E., 2010, *ApJ*, **715**, L138
- Bell E. F., McIntosh D. H., Katz N., Weinberg M. D., 2003, *ApJS*, **149**, 289
- Belloni D., Giersz M., Askar A., Leigh N., Hypki A., 2016, *MNRAS*, **462**, 2950
- Belokurov V., Sanders J. L., Fattahi A., Smith M. C., Deason A. J., Evans N. W., Grand R. J. J., 2020, *MNRAS*, **494**, 3880
- Binney J., Tremaine S., 2008, *Galactic Dynamics: Second Edition*. Princeton University Press
- Breen P. G., Heggie D. C., 2011, *MNRAS*, **420**, 13
- Breen P. G., Heggie D. C., 2013, *MNRAS*, **432**, 2779
- Breivik K., et al., 2020, *ApJ*, **898**, 71
- Brodie J. P., Strader J., 2006, *ARAA*, **44**, 193
- Brown G., Gnedin O. Y., 2021, arXiv e-prints, p. [arXiv:2106.12420](https://arxiv.org/abs/2106.12420)
- Caldwell N., Schiavon R., Morrison H., Rose J. A., Harding P., 2011, *AJ*, **141**, 61
- Chatterjee S., Fregeau J. M., Umbreit S., Rasio F. A., 2010, *ApJ*, **719**, 915
- Chernoff D. F., Weinberg M. D., 1990, *ApJ*, **351**, 121
- Claeys J. S. W., Pols O. R., Izzard R. G., Vink J., Verbunt F. W. M., 2014, *Astronomy & Astrophysics*, **563**, A83
- Dotter A., et al., 2010, *ApJ*, **708**, 698
- Dotter A., Sarajedini A., Anderson J., 2011, *ApJ*, **738**, 74
- Duquennoy A., Mayor M., 1991, *A&A*, **500**, 337
- Elson R. A. W., Fall S. M., Freeman K. C., 1987, *ApJ*, **323**, 54
- Elson R. A. W., Freeman K. C., Lauer T. R., 1989, *ApJ*, **347**, L69
- Forbes D. A., Bridges T., 2010, *MNRAS*, **404**, 1203
- Forbes D. A., et al., 2018, *Proceedings of the Royal Society of London Series A*, **474**, 20170616
- Fregeau J. M., Rasio F. A., 2007, *ApJ*, **658**, 1047
- Freitag M., 2008, *The Cambridge N-Body Lectures*. Vol. 760, Springer Netherlands, Dordrecht, doi:10.1007/978-1-4020-8431-7, <http://www.springerlink.com/index/10.1007/978-1-4020-8431-7>
- Freitag M., Benz W., 2001, *A&A*, **375**, 711
- Fryer C. L., Kalogera V., 2001, *ApJ*, **554**, 548
- Fryer C. L., Belczynski K., Wiktorowicz G., Dominik M., Kalogera V., Holz D. E., 2012, *ApJ*, **749**, 91
- Fukushige T., Heggie D. C., 2000, *MNRAS*, **318**, 753
- Gao B., Goodman J., Cohn H., Murphy B., 1991, *ApJ*, **370**, 567
- Gieles M., Zwart S. F. P., Baumgardt H., Athanassoula E., Lamers H. J. G. L. M., Sipior M., Leenaarts J., 2006, *MNRAS*, **371**, 793
- Gieles M., Athanassoula E., Portegies Zwart S. F., 2007, *MNRAS*, **376**, 809
- Gieles M., Baumgardt H., Heggie D. C., Lamers H. J. G. L. M., 2010, *MNRAS*, **408**, L16
- Gieles M., Heggie D. C., Zhao H., 2011, *MNRAS*, **413**, 2509
- Giersz M., Heggie D. C., 2011, *MNRAS*, **410**, 2698
- Giersz M., Heggie D. C., Hurley J. R., 2008, *MNRAS*, **388**, 429
- Giersz M., Heggie D. C., Hurley J. R., Hypki A., 2013, *MNRAS*, **431**, 2184
- Gnedin O. Y., Ostriker J. P., 1997, *ApJ*, **474**, 223
- Gnedin O. Y., Ostriker J. P., 1999, *ApJ*, **513**, 626
- González E., Kremer K., Chatterjee S., Fragione G., Rodriguez C. L., Weatherford N. C., Ye C. S., Rasio F. A., 2021, *ApJ*, **908**, L29
- Grudić M. Y., Kruijssen J. M. D., Faucher-Giguère C.-A., Hopkins P. F., Ma X., Quataert E., Boylan-Kolchin M., 2021, *MNRAS*, **506**, 3239
- Grudić M. Y., Hafen Z., Rodriguez C. L., Guszejnov D., Lamberts A., Wetzel A., Boylan-Kolchin M., Faucher-Giguère C.-A., 2022, arXiv e-prints, p. [arXiv:2203.05732](https://arxiv.org/abs/2203.05732)
- Grudić M. Y., Guszejnov D., Hopkins P. F., Lamberts A., Boylan-Kolchin M., Murray N., Schmitz D., 2018, *MNRAS*, **481**, 688
- Gurvich A. B., 2021, FIRE Studio: Movie making utilities for the FIRE simulations, doi:2022ascl.soft02006G, https://github.com/agurvich/FIRE_studio
- Gurvich A. B., et al., 2022, arXiv e-prints, p. [arXiv:2203.04321](https://arxiv.org/abs/2203.04321)
- Guszejnov D., Grudić M. Y., Offner S. S. R., Boylan-Kolchin M., Faucher-Giguère C.-A., Wetzel A., Benincasa S. M., Loebman S., 2020, *MNRAS*, **492**, 488
- Hafen Z., et al., 2022, *MNRAS*, **514**, 5056
- Harris W. E., 1996, *AJ*, **112**, 1487
- Harris W. E., 2010, *Philosophical transactions. Series A, Mathematical, physical, and engineering sciences*, **368**, 889
- Harris W. E., Harris G. L. H., Alessi M., 2013, *ApJ*, **772**, 82
- Harris W. E., Blakeslee J. P., Harris G. L. H., 2017, *ApJ*, **836**, 67
- Heggie D. C., 2014, *MNRAS*, **445**, 3435
- Heggie D. C., Giersz M., 2014, *MNRAS*, astro-ph.G, 2459
- Heggie D. C., Trenti M., Hut P., 2006, *MNRAS*, **368**, 677
- Hénon M., 1961, *Annales d’Astrophysique*, **24**, 369
- Henon M., 1969, *A&A*, **2**, 151
- Hobbs G., Lorimer D. R., Lyne A. G., Kramer M., 2005, *MNRAS*, **360**, 974
- Hopkins P. F., 2017, arXiv:1712.01294 [astro-ph, physics:physics]
- Hopkins P. F., Kereš D., Oñorbe J., Faucher-Giguère C.-A., Quataert E., Murray N., Bullock J. S., 2014, *MNRAS*, **445**, 581
- Hopkins P. F., et al., 2018, *MNRAS*, **480**, 800
- Hopkins P. F., et al., 2020, *MNRAS*, **492**, 3465
- Hurley J. R., Pols O. R., Tout C. A., 2000, *MNRAS*, **315**, 543
- Hurley J. R., Tout C. A., Aarseth S. J., Pols O. R., 2001, *MNRAS*, **323**, 630
- Hurley J. R., Tout C. A., Pols O. R., 2002, *MNRAS*, **329**, 897
- Hénon M., 1971a, *Astrophysics and Space Science*, **13**, 284
- Hénon M., 1971b, *Astrophysics and Space Science*, **14**, 151
- Inagaki S., Saslaw W. C., 1985, *ApJ*, **292**, 339
- Joshi K. J., Rasio F. A., Zwart S. P., Portegies Zwart S., 2000, *ApJ*, **540**, 969
- Kiel P. D., Hurley J. R., 2009, *MNRAS*, **395**, 2326
- King I., 1959, *AJ*, **64**, 351
- King I. R., 1966, *AJ*, **71**, 276
- Kremer K., Ye C. S., Chatterjee S., Rodriguez C. L., Rasio F. A., 2018, *ApJ*, **855**, L15
- Kremer K., Chatterjee S., Ye C. S., Rodriguez C. L., Rasio F. A., 2019, *ApJ*, **871**, 38
- Kremer K., et al., 2020a, *ApJS*, **247**, 48
- Kremer K., et al., 2020b, *ApJ*, **903**, 45
- Kroupa P., 2001
- Kroupa P., 2008, *Initial Conditions for Star Clusters*. p. 181, doi:10.1007/978-1-4020-8431-7_8
- Kruijssen J. M. D., 2014, *Classical and Quantum Gravity*, **31**, 244006
- Kruijssen J. M. D., 2015, *MNRAS*, **454**, 1658
- Kruijssen J. M. D., Pelupessy F. I., Lamers H. J. G. L. M., Portegies Zwart S. F., Icke V., 2011, *MNRAS*, **414**, 1339
- Kruijssen J. M. D., Pfeffer J. L., Reina-Campos M., Crain R. A., Bastian N., 2019, *MNRAS*, **486**, 3180
- Kundic T., Ostriker J. P., 1995, *ApJ*, **438**, 702
- Küpper A. H. W., Maschberger T., Kroupa P., Baumgardt H., 2011, *MNRAS*, **417**, 2300
- Küpper A. H. W., Lane R. R., Heggie D. C., 2012, *MNRAS*, **420**, 2700
- Lacey C., Cole S., 1993, *MNRAS*, **262**, 627
- Larsen S. S., 2010, *Philosophical Transactions of the Royal Society of London Series A*, **368**, 867
- Larsen S. S., Richtler T., 1999, *A&A*, **345**, 59
- Larsen S. S., Richtler T., 2004, *A&A*, **427**, 495
- Lauer T. R., Faber S. M., Ajhar E. A., Grillmair C. J., Scowen P. A., 1998, *AJ*, **116**, 2263
- Li H., Gnedin O. Y., 2019, *MNRAS*, **486**, 4030
- Li H., Gnedin O. Y., Gnedin N. Y., Meng X., Semenov V. A., Kravtsov A. V., 2017, *ApJ*, **834**, 69
- Li H., Gnedin O. Y., Gnedin N. Y., 2018, *ApJ*, **861**, 107
- Linden S. T., et al., 2021, *ApJ*, **923**, 278
- Long K., Ostriker J. P., Aguilar L., 1992, *ApJ*, **388**, 362
- Ma X., Hopkins P. F., Wetzel A. R., Kirby E. N., Anglés-Alcázar D., Faucher-Giguère C.-A., Kereš D., Quataert E., 2017, *MNRAS*, **467**, 2430
- Ma L., Hopkins P. F., Ma X., Anglés-Alcázar D., Faucher-Giguère C.-A., Kelley L. Z., 2021, *MNRAS*, **508**, 1973
- Mackey A. D., Gilmore G. F., 2003a, *MNRAS*, **338**, 85
- Mackey A. D., Gilmore G. F., 2003b, *MNRAS*, **338**, 120

- Mackey A. D., Wilkinson M. I., Davies M. B., Gilmore G. F., 2008, *MNRAS*, 386, 65
- Madrid J. P., Leigh N. W. C., Hurley J. R., Giersz M., 2017, *MNRAS*, 470, 1729
- Maliszewski K., Giersz M., Gondek-Rosińska D., Askar A., Hypki A., 2021, arXiv e-prints, p. [arXiv:2111.09223](https://arxiv.org/abs/2111.09223)
- Meng X., Gnedin O. Y., 2022, *MNRAS*, 515, 1065
- Merritt D., Piatek S., Portegies Zwart S., Hemsendorf M., 2004, *ApJ*, 608, L25
- Miyamoto M., Nagai R., 1975, *PASJ*, 27, 533
- Moe M., Kratter K. M., Badenes C., 2019, *ApJ*, 875, 61
- Morscher M., Umbreit S., Farr W. M., Rasio F. A., 2013, *ApJ*, 763, L15
- Morscher M., Pattabiraman B., Rodríguez C., Rasio F. A., Umbreit S., 2015, *ApJ*, 800, 9
- Neumayer N., Seth A., Böker T., 2020, *A&ARv*, 28, 4
- Ostriker J. P., Caldwell J. A. R., 1983, in Shuter W. L. H., ed., *Astrophysics and Space Science Library* Vol. 100, Kinematics, Dynamics and Structure of the Milky Way. pp 249–257, doi:[10.1007/978-94-009-7060-1_35](https://doi.org/10.1007/978-94-009-7060-1_35)
- Ostriker J. P., Spitzer Lyman J., Chevalier R. A., 1972, *ApJ*, 176, L51
- Pattabiraman B., Umbreit S., Liao W.-k., Choudhary A., Kalogera V., Memik G., Rasio F. A., 2013, *ApJS*, 204, 15
- Peacock M. B., Maccarone T. J., Knigge C., Kundu A., Waters C. Z., Zepf S. E., Zurek D. R., 2010, *MNRAS*, 402, 803
- Pfeffer J., Kruijssen J. M. D., Crain R. A., Bastian N., 2018, *MNRAS*, 475, 4309
- Plummer H. C., 1911, *MNRAS*, 71, 460
- Portegies Zwart S. F., Baumgardt H., Hut P., Makino J., McMillan S. L. W., 2004, *Nature*, 428, 724
- Portegies Zwart S. F., McMillan S. L., Gieles M., 2010, *ARAA*, 48, 431
- Price-Whelan A. M., 2017, *The Journal of Open Source Software*, 2
- Prieto J. L., Gnedin O. Y., 2008, *ApJ*, 689, 919
- Renaud F., Gieles M., 2015, *MNRAS*, 448, 3416
- Renaud F., Gieles M., Boily C. M., 2011, *MNRAS*, 418, 759
- Richtler T., Bassino L. P., Dirsch B., Kumar B., 2012, *A&A*, 543, A131
- Rieder S., Pelupessy I., 2019, *rieder/Fresco: Fresco 0.6*, doi:[10.5281/zenodo.3553805](https://doi.org/10.5281/zenodo.3553805), <https://doi.org/10.5281/zenodo.3553805>
- Rieder S., Ishiyama T., Langelan P., Makino J., McMillan S. L. W., Portegies Zwart S., 2013, *MNRAS*, 436, 3695
- Rodríguez C. L., Chatterjee S., Rasio F. A., 2016a, *Phys. Rev. D*, 93, 084029
- Rodríguez C. L., Morscher M., Wang L., Chatterjee S., Rasio F. A., Spurzem R., 2016b, *MNRAS*, 463, 2109
- Rodríguez C. L., Zevin M., Pankow C., Kalogera V., Rasio F. A., 2016c, *ApJ*, 832, L2
- Rodríguez C. L., Amaro-Seoane P., Chatterjee S., Kremer K., Rasio F. A., Samsing J., Ye C. S., Zevin M., 2018a, *Phys. Rev. D*, 98, 123005
- Rodríguez C. L., Amaro-Seoane P., Chatterjee S., Rasio F. A., 2018b, *Phys. Rev. Lett.*, 120, 151101
- Rodríguez C. L., et al., 2020, *ApJ*, 896, L10
- Rodríguez C. L., et al., 2022, *ApJS*, 258, 22
- Rui N. Z., Kremer K., Weatherford N. C., Chatterjee S., Rasio F. A., Rodríguez C. L., Ye C. S., 2021a, *NicholasRui/cmctoolkit: First release*, doi:[10.5281/zenodo.4579950](https://doi.org/10.5281/zenodo.4579950)
- Rui N. Z., Kremer K., Weatherford N. C., Chatterjee S., Rasio F. A., Rodríguez C. L., Ye C. S., 2021b, *ApJ*, 912, 102
- Ryon J. E., et al., 2015, *MNRAS*, 452, 525
- Samsing J., D’Orazio D. J., Kremer K., Rodríguez C. L., Askar A., 2020, *Phys. Rev. D*, 101, 123010
- Santistevan I. B., Wetzell A., El-Badry K., Bland-Hawthorn J., Boylan-Kolchin M., Bailin J., Faucher-Giguère C.-A., Benincasa S., 2020, *MNRAS*, 497, 747
- Schödel R., Gallego-Cano E., Dong H., Noguerras-Lara F., Gallego-Calvente A. T., Amaro-Seoane P., Baumgardt H., 2018, *A&A*, 609, A27
- Sollima A., Mastrobuono Battisti A., 2014, *MNRAS*, 443, 3513
- Spitzer Lyman J., 1958, *ApJ*, 127, 17
- Spitzer L., 1987, Princeton, NJ, Princeton University Press, 1987, 191 p.
- Spitzer Lyman J., Hart M. H., 1971, *ApJ*, 164, 399
- Stern J., et al., 2021, *ApJ*, 911, 88
- Terlevich E., 1987, *MNRAS*, 224, 193
- Trager S. C., King I. R., Djorgovski S., 1995, *AJ*, 109, 218
- Tremaine S. D., Ostriker J. P., Spitzer L. J., 1975, *ApJ*, 196, 407
- Tremmel M., Governato F., Volonteri M., Quinn T. R., 2015, *MNRAS*, 451, 1868
- Trenti M., Heggie D. C., Hut P., 2007, *MNRAS*, 374, 344
- VandenBerg D. A., Brogaard K., Leaman R., Casagrande L., 2013, *ApJ*, 775, 134
- Vasiliev E., Baumgardt H., 2021, *MNRAS*, 505, 5978
- Vesperini E., Heggie D. C., 1997, *MNRAS*, 289, 898
- Vesperini E., McMillan S. L. W., Portegies Zwart S., 2009, *ApJ*, 698, 615
- Vink J. S., de Koter A., Lamers H. J. G. L. M., 2001, *A&A*, 369, 574
- Wang C., Jia K., Li X.-D., 2016a, p. 10
- Wang L., et al., 2016b, *MNRAS*, 458, 1450
- Wang L., Iwasawa M., Nitadori K., Makino J., 2020, *MNRAS*, 497, 536
- Weatherford N. C., Chatterjee S., Kremer K., Rasio F. A., 2020, *ApJ*, 898, 162
- Webb J. J., Harris W. E., Sills A., Hurley J. R., 2013, *ApJ*, 764, 124
- Webb J. J., Sills A., Harris W. E., Hurley J. R., 2014, *MNRAS*, 445, 1048
- Weinberg M. D., 1994a, *AJ*, 108, 1398
- Weinberg M. D., 1994b, *AJ*, 108, 1403
- Weinberg M. D., 1994c, *AJ*, 108, 1414
- Wetzell A. R., Hopkins P. F., Kim J.-h., Faucher-Giguère C.-A., Kereš D., Quataert E., 2016, *ApJ*, 827, L23
- Wilkinson M. I., Hurley J. R., Mackey A. D., Gilmore G. F., Tout C. A., 2003, *MNRAS*, 343, 1025
- Ye C. S., Kremer K., Rodríguez C. L., Rui N. Z., Weatherford N. C., Chatterjee S., Fragione G., Rasio F. A., 2021, arXiv e-prints, p. [arXiv:2110.05495](https://arxiv.org/abs/2110.05495)
- Yu S., et al., 2021, *MNRAS*, 505, 889
- Zinn R., 1985, *ApJ*, 293, 424
- van der Marel R. P., Sigurdsson S., Hernquist L., 1997, *ApJ*, 487, 153

APPENDIX A: TIDAL STRIPPING IN SPHERICAL N -BODY CODES

While CMC has been shown to produce extremely accurate models of spherical star clusters (when compared to direct N -body integrators), a large part of the speed of the method derives from the assumption of spherical symmetry. Of course, the application of an external tidal potential is explicitly non-spherical. For direct N -body integrators, this does not pose a significant issue: the external field can either be incorporated into the cluster using the instantaneous tidal tensor (e.g., [Renaud et al. 2011](#)), or directly using the galactic potential itself (e.g. [Renaud & Gieles 2015](#); [Wang et al. 2020](#)), with the external force being added directly to the equations of motion. However, for CMC (and other approaches that rely on spherical symmetry), the forces cannot be added in 3 dimensions self-consistently, which prohibits us from calculating when stars move beyond the classic Roche-Lobe shape of the energy surface.

What Equation (5) provides us with is the distance from the cluster center to the L1 Lagrange point of the cluster-galaxy system where the combined gravitational influence of both potentials and the centrifugal force from the cluster’s galactic orbit sum to zero (while neglecting the Coriolis and Eulerian pseudo forces that arise in the rotating reference frame of the cluster). We assess two methods of implementing tidal stripping. The most naive way to impose this tidal boundary on our clusters would be to simply remove any stars whose apocenter lies beyond that tidal boundary. However as stated in §2.4 the criterion for whether a star is bound to the cluster relies on the energy of the orbit, not its position. As such, detailed comparisons to direct N -body simulations have suggested that a modified energy criterion, where any stars with energies greater

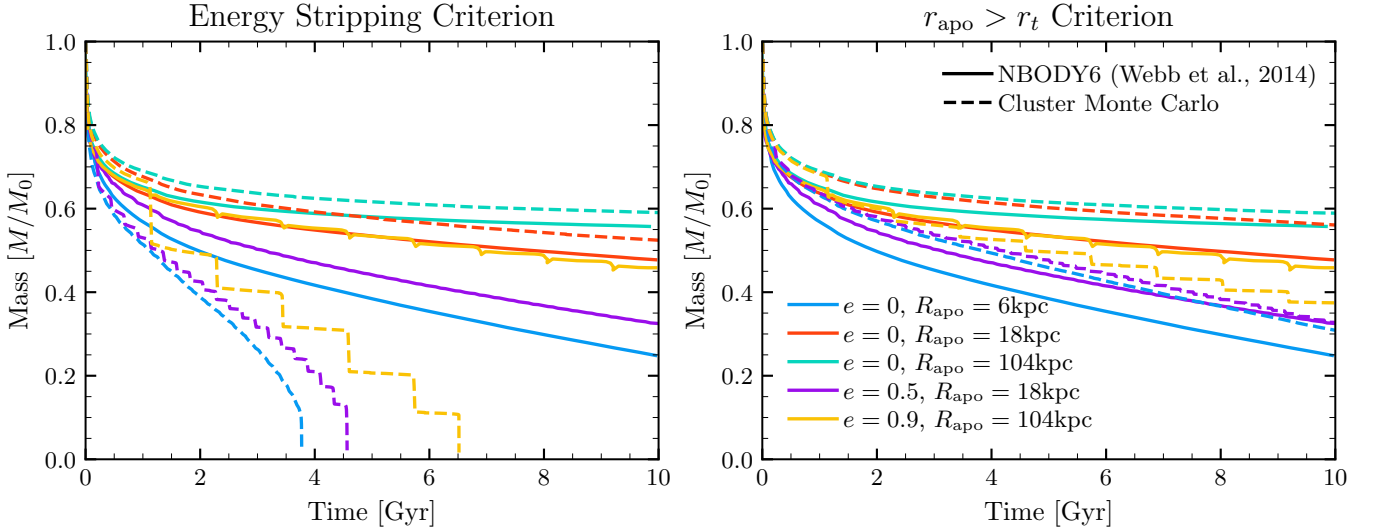


Figure A1. Comparison between direct N -body simulations of Webb et al. (2014) and CMC models evolved with the same initial conditions, galactic potential, and orbit. The different colors correspond to orbits with different eccentricities (e) and apogalacticons (R_{apo}) in the galactic potential described in the text. On the **left**, we show the normalized mass loss rates for both approaches using the energy criterion of tidal mass loss from Giersz et al. (2008), while on the **right** we show the same using the more simplistic radial criterion, where any stars with $r_{\text{apo}} > r_t$ are stripped. Surprisingly, the radial criterion matches the N -body mass loss rates significantly better than the default energy criterion, and as such we adopt it for this study. Note that the N -body models on highly-eccentric orbits show apparent mass gain after they pass through perigalacticon. This reflects the recapture of stars by the cluster potential after a close perigalactic passage (e.g. Küpper et al. 2012), which cannot be modeled in CMC at present.

than $\alpha\phi_t$ are stripped from the cluster, is often the preferred approach to tidal stripping (Giersz et al. 2008; Chatterjee et al. 2010). Here, ϕ_t is the potential of the cluster at the tidal boundary r_t defined in Equation (5), and α is a parameter tuned to direct N -body simulations, given by

$$\alpha = 1.5 - 3 \left(\frac{\log(\Lambda)}{N} \right)^{1/4} \quad (\text{A1})$$

This is the default prescription in both CMC and the MOCCA codes, and has been shown to reproduce the mass loss rates of clusters on circular orbits (Rodríguez et al. 2016c).

To ensure that our implementation of the tidal tensor in CMC can have similar success, we compare the results of idealized Monte Carlo integrations to direct N -body models from Webb et al. (2014). In that work, the authors used NBODY6 (Aarseth 2003) to explore the influence of non-circular galactic orbits on the mass loss rates from idealized models of star clusters (comprised of equal-mass point particles). They consider 5 different orbits with varying eccentricities and pericenters in a galactic potential consisting of a disk, bulge, and halo with the default parameters from NBODY6; we reproduce this potential using a potential comprised of a $1.5 \times 10^{10} M_{\odot}$ Keplerian potential for the bulge/SMBH, a logarithmic potential that yields a velocity of 220 km/s at 8.5 Kpc from the galactic center, and a Miyamoto & Nagai (1975) disk potential with mass $5 \times 10^{10} M_{\odot}$ and scale parameters $a = 4.5$ Kpc and $b = 0.5$ Kpc. The orbits are integrated using the Ga1a (Price-Whelan 2017) package, which also allows us to extract the tidal tensor at each point along the orbit. This is then fed directly into CMC, allowing us to reproduce the initial conditions of Webb et al. (2014).

In Fig. 2, we show the normalized mass loss rates over time for our 5 CMC models and the N -body models from Webb et al. (2014), using both the basic radial stripping criterion and the more sophisticated energy-based criterion of Giersz et al. (2008). Surprisingly,

the radial criterion shows better agreement with the NBODY6_tt models than the default energy criterion, which causes the CMC models to lose mass faster and disrupt sooner than their N -body counterparts. We speculate that this is because the radial criterion, by depending on the apocenter of each star’s orbit, requires diffusion in both energy and angular momentum for a star’s apocenter to move beyond the cluster boundary (while the energy criterion requires only the former). However, further study will be required to confirm this. For this work, we use the radial criterion, and strip any stars where $r_{\text{apo}} > r_t$.

We reiterate that both approaches to tidal stripping we present here are highly simplified. In practice, the escape of stars from a star cluster is a very complicated problem even in a fixed tidal field. The time scale for stars that are technically unbound to escape from the cluster is non-trivial to calculate, and during that time, stars may linger indefinitely in unstable orbits near the Lagrange points (even though $E > \alpha\phi_t$; e.g., Henon 1969; Fukushige & Heggie 2000), or may be scattered back to lower energies (e.g., King 1959; Baumgardt 2001). To account for this, recent improvements to the Monte Carlo method (Giersz et al. 2013; Sollima & Mastrobuono Battisti 2014) have implemented more sophisticated techniques which calculate approximate timescales for the stars to escape their parent clusters, which in turn treats escaping particles as a Poisson process. However, even with this sophisticated approach, the escape rate from Monte Carlo methods still overestimates the rate from direct N -body calculations (e.g., Madrid et al. 2017, Fig. 5). Furthermore, these effects are all compounded by the presence of a time-varying galactic potential, which changes the position of the Lagrange points over time. It is not obvious that these improvements, while more physically motivated, would necessarily improve the comparisons in Fig. 2. Work to better compare the escape rate we have calculated to direct N -body calculations is currently underway.

APPENDIX B: TIDAL SHOCKING

While we have incorporated time-varying tidal forces based on the above implementation, we have neglected the effect of tidal shocking, where the time-dependent external potential can itself do work on the cluster itself. These shocks both directly inject energy into the cluster, thereby increasing its radius (and susceptibility to tidal stripping), while second-order effects can serve to advance the relaxation-driven evolution of the cluster (Kundic & Ostriker 1995), speeding it towards an early demise. It has been argued that the inclusion of tidal shocking is critical to explain the destruction of massive clusters with large radii (e.g., Gnedin & Ostriker 1997).

We showed the vital diagrams used in Gnedin & Ostriker (1997) as evidence of the importance of tidal shocking in Fig. 15. However, from that plot, it was not immediately obvious that tidal shocking was actually a necessary component for reproducing the mass and radii of present-day GCs in the MW, since only a handful of clusters were born in the region excluded by tidal shocking, and the majority of those were destroyed by tidal stripping anyway. However, the fact that our clusters largely inhabit the correct regions predicted by the MW vital diagrams is not proof that tidal shocking is negligible.

While implementing tidal shocking in a Hénon-style N -body code presents significant challenges, we can estimate what the influence of tidal shocking would have been in our population in the following way: first, during each shock, we can compute the average change in stellar energies per unit mass at the half-mass radius, r_{hm} , of the cluster with (Prieto & Gnedin 2008):

$$\langle \Delta E_h \rangle = \frac{1}{6} I_{\text{tid}} r_{\text{hm}}^2 \quad (\text{B1})$$

where I_{tid} is the tidal heating parameter, given by

$$I_{\text{tid}} = \sum_{i,j} \left(\int \mathbf{T}^{ij} dt \right)^2 \left(1 + \left(\frac{\tau}{t_{\text{dyn}}} \right)^2 \right)^{-3/2} \quad (\text{B2})$$

where the sum is over all components i, j , of the tidal tensor defined in Equation (4). The second term in the parenthesis is the adiabatic correction, accounting for the ability of the clusters to successfully re-absorb injected energy. We use the power-law adiabatic correction from (Gnedin & Ostriker 1999), which depends on the ratio of the length of the tidal shock τ to the dynamical time of the cluster t_{dyn} . Once we have the average energy injected by every tidal shock, we can convert this to a typical mass loss experienced by the cluster due to its subsequent expansion. We use the approximate relation from Gieles et al. (2006):

$$\frac{\Delta M}{M_0} \approx 0.22 \frac{\langle \Delta E_h \rangle}{E_0} \quad (\text{B3})$$

where M_0 and E_0 are the initial mass and energy of the cluster.

As an order-of-magnitude check, we assume that once the cumulative mass loss given by Equation (B3) exceeds the total mass, the cluster has been disrupted. For every cluster in our evolved catalog, we identify tidal shocks as occurring whenever any component of the tidal tensor is one standard deviation away from the median value of that component as measured over the entire cluster lifetime (Fig. 1 shows the typical amount by which the effective tidal tensor changes). The integral in Equation (B2) is then calculated by directly summing the component of each shock times the Δt between the FIRE snapshots that Equation (4) was extracted from. In practice, the vast majority of shocks only appear in a single snapshot,

so we multiply each component by the spacing between snapshots (≈ 20 -30 Myr).

After applying this procedure to our catalog, we found virtually no contribution to our final cluster population arising from our neglect of tidal shocking. In fact, according to this procedure, only one of our 895 clusters should have been destroyed by tidal shocking, and even in that case—a particularly massive ($\sim 3 \times 10^6 M_{\odot}$) and large ($r_{\text{hm}} = 26$ pc) cluster—it was destroyed by tidal shocking at the same time CMC recorded it as being destroyed by tidal stripping. In other words, the strong tidal fields responsible for shocking the cluster are also responsible for the increase in mass loss through the tidal boundary.

From this, one might conclude that our implementation of tidal stripping in CMC naturally culls large clusters at the same rate as tidal shocking would, since they are both based in the rapid variation of the galactic tidal field, allowing us to reproduce the correct distribution of clusters in the mass-radius region as Gnedin & Ostriker (1997). However, such optimism would be premature. As previously mentioned, we have extracted our tidal tensors from snapshots of the m12i galaxy that are typically taken every 20-30 Myr. But the typical dynamical time of any of our clusters during a tidal shocks is a significantly shorter (~ 1 Myr), and as a result, each tidal shock is reduced by a factor of 10^4 from the adiabatic correction to Equation (B2).

What this actually means is that the 20 Myr interval between snapshots is insufficient to resolve the influence of tidal shocking on the star cluster population of a single galaxy. Work to improve the extraction of the instantaneous tidal boundaries in zoom in simulations, as well as comparisons to direct N -body models capable of resolving the influence of tidal shocking on the cluster survival, is currently underway.